arXiv:cond-mat/0509033v1 [cond-mat.soft] 1 Sep 2005

# Model for Polymorphic Transitions in Bacterial Flagella

Srikanth V. Srigiriraju and Thomas R. Powers
*Division of Engineering, Box D, Brown University, Providence, RI 02912*

(Dated: 16 August 2005)

Many bacteria use rotating helical flagellar filaments to swim. The filaments undergo polymorphic transformations in which the helical pitch and radius change abruptly. These transformations arise in response to mechanical loading, changes in solution temperature and ionic strength, and point substitutions in the amino acid sequence of the protein subunits that make up the filament. To explain polymorphism, we propose a new coarse-grained continuum rod theory based on the quaternary structure of the filament. The model has two molecular switches. The first is a double-well potential for the extension of a protofilament, which is one of the eleven almost longitudinal columns of subunits. Curved filament shapes occur in the model when there is a mismatch strain, i.e. when inter-subunit bonds in the inner core of the filament prefer a subunit spacing which is intermediate between the two spacings favored by the double-well potential. The second switch is a double-well potential for twist, due to lateral interactions between neighboring protofilaments. Cooperative interactions between neighboring subunits within a protofilament are necessary to ensure the uniqueness of helical ground states. We calculate a phase diagram for filament shapes and the response of a filament to external moment and force.

## I. INTRODUCTION

Allosteric proteins switch between different conformations in response to the binding of ligands. Allostery underlies a wide range of cellular processes, such as the cooperative binding of oxygen to hemoglobin [1], the negative feedback control of the DNA-binding *trp* repressor in *Escherichia coli* [2], and the regulation of the catalyst aspartate transcarbamoylase, also in *E. coli* [3]. All these examples involve conformational changes of a small molecule in response to the the binding of a ligand. Bray and Duke have recently argued that the concept of allostery should be extended from small molecules to large assemblies of proteins, in which conformational change propagates through a one- or two-dimensional lattice [4]. In this picture of "conformational spread," the state of an individual protein subunit of a large assembly is stabilized either by ligand binding *or* by the conformational state of a neighboring subunit.

In this article we develop a theory based on conformational spread for polymorphic transformations of the flagellar filaments of bacteria such as *E. coli.* These filaments are hollow tubes built from identical protein subunits known as flagellin [5]. To explain why the tubes are usually helical, instead of straight cylinders, Asakura supposed that each flagellin subunit can be in one of two distinct conformations, with one slightly longer than the other [6]. Since the subunits may be grouped into eleven protofilaments which slowly wind around each other to form the filament, a helical filament shape arises when some of the protofilaments consist of only long subunits, and the rest consist of only short subunits. For example, for physiological solution conditions and in the absence of external forces and moments, the filament of *E. coli* is left-handed with a pitch of $2.5\,\mu$m and a diameter of $0.4\,\mu$m [7]. Indirect evidence of the spread of conformational change comes from the response of a helix to hydrodynamic torque, which can trigger a polymorphic transition from a left-handed normal state to a right-handed state [8]. For example, Hotani has detached filaments from *Salmonella typhimurium* cells and used hydrodynamic torque to trigger polymorphic transformations [9]. A rotating helix in a viscous fluid generates propulsive thrust; conversely, flow directed along the axis of a helix not only stretches the helix, but also tends to untwist the helix, independent of its handedness. By flowing solution past filaments stuck at one end to a microscope slide, Hotani observed different helical states propagating from the stuck end to the free end [9].

Polymorphic transitions caused by hydrodynamic torque also occur in free-swimming bacteria [8]. There are usually five to six flagella per cell. When the flagellar motors turn counterclockwise (as viewed from outside the cell), the left-handed helices wrap into a bundle which propels the cell forward [10, 11]. Reversal of the rotation direction of a motor leads to a sequence of events in which the corresponding filament unwinds from the bundle and transforms to a right-handed state [8], before eventually wrapping up into the bundle once the motor returns to counterclockwise rotation. Fluorescent labelling of the filaments has recently revealed the precise dynamics of this process [7]. The typical sequence begins with a transformation from the left-handed normal state to a right-handed "semi-coiled" state with half the helical pitch of the normal state. This transformation changes the swimming direction of the cell. Then there is an additional transformation to a right-handed state called "curly-1," which has a similar pitch but roughly half the radius of the semi-coiled state. When the motor reverses back to counterclockwise rotation, the filament transforms directly to the normal state.

Discontinuous transitions among these states can also occur due to changes in pH [12], salt concentration [12], or temperature [13]. Straight states [6] and curved planar ("coiled") states [12] have also been observed.

In this article we describe a continuum model for flag-

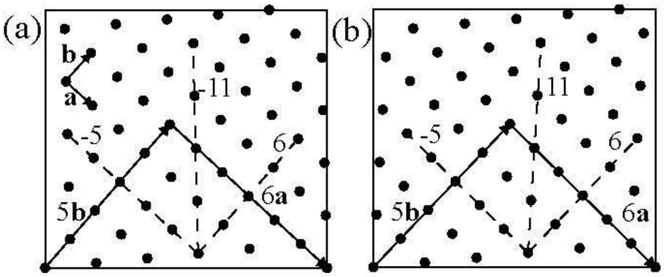

FIG. 1: The lattices of (a) L-type and (b) R-type filaments, at radius $a = 4.5\,\text{nm}$ and using data from [15]. The vertical edges are identified. Note the 11-, 6-, and 5-start helices. The protofilaments are the 11-start helices.

ellar filaments. We begin in section II with a review of experiments that reveal the structure and mechanical response of the flagellar filament, and then discuss previous theoretical models for polymorphism. We introduce our model in section III. The essential features of our model are two inequivalent subunit conformations, a mismatch of the preferred spacing of protein domains in the inner and outer core of the filament, and cooperative interactions between neighboring subunits. All three of these features are suggested by the experiments, and are required for our model to yield a unique helical ground state for given parameters. In section IV we study a simplified version of our model, introduced in [14], which neglects extensibility and twist-stretch interactions. Using this model, we calculate the filament ground states as a function of material parameters. Then we turn to the response of the filament to external moment. Some of these results were described in [14]. We conclude this section with new calculations of the response to external force. In section V, we present the phase diagram and response to external moments and forces for the full model, in which the simplifying assumptions of section IV are removed. We discuss our results in section VI.

## II. SUMMARY OF PREVIOUS WORK.

Before the detailed structures of virus capsids were measured, it was argued that self-assembly of identical subunits would lead to highly symmetric forms, with all subunits in equivalent bonding environments [16]. For example, the protective coat of tobacco mosaic virus consists of identical protein subunits which form a straight cylinder [17]. In flagella, the flagellin subunits also form a two-dimensional crystal on the surface of a cylinder, which is about 20 nm in diameter. As mentioned already, the subunits can be grouped into eleven protofilaments that gradually wind around each other to form the filament. Since the flagellum usually has a helical shape, exact equivalence cannot apply. However, since the filament is thin, small departures from exact equivalence can lead to helices of the observed dimensions [6].

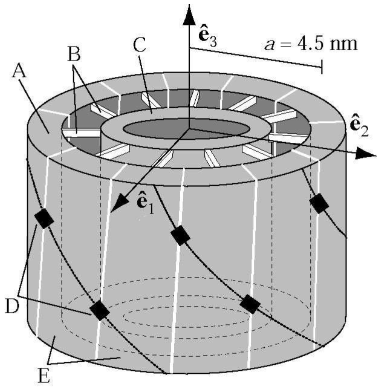

FIG. 2: Cartoon of a short segment of the R-type flagellar filament, showing the outer core (A), connecting spokes (B), inner core (C), and lateral bonds (D) between neighboring protofilaments (E). The position of the spokes is not accurate, and is only meant to indicate that the inner and outer cores are connected. The outer domains are not shown. The lateral bonds lie along the five 5-start helices.

### A. Experiments

A consequence of Asakura's picture [6] of two stable states for protofilaments is that two distinct straight filaments are possible, one in which all protofilaments are short, and one in which all are long. These states, known as R-type and L-type, have been observed [18]. The subunit period along a protofilament is 0.8 Å shorter in R-type than in L-type. The protofilaments make a positive angle with the longitudinal direction in R-type, leading to right-handed twist, whereas the protofilaments in L-type have a left-handed twist. Figures 1 (a) and (b) show the subunit lattices in L- and R-type at a radius of 4.5 nm, obtained from x-ray scattering from fibers of filaments [15]. The primitive lattice vectors $\mathbf{a}$ and $\mathbf{b}$ in the two figures are slightly different, but in both cases $6\mathbf{a} + 5\mathbf{b} = C\hat{\mathbf{x}}$ where $C$ is the circumference of the filament at 4.5 nm, and $C\hat{\mathbf{x}} = \mathbf{0}$ since the lattices lie on the surface of a cylinder. The vector constraint on the two lattice vectors yields two degrees of freedom, which may be taken to be the subunit spacing along the 11-start direction and the angle the 11-start direction makes with a longitude. Equivalently, we may replace the angle degree of freedom with the twist of the filament.

Electron microscopy has shown that the filament cross-section consists of outer domains surrounding a core with inner and outer parts (Fig. 2) [19]. The inner and outer cores are connected by radial spokes. The outer domains do not seem to affect the mechanical properties of the filament; for example, mutations in the outer domain do not affect polymorphism [20]. Both the outer core and the inner core are crucial for polymorphism. Mutations in the outer core can change the ground state of the filament from normal to curly, semi-coiled, or straight [21]. Without the inner core, there is no polymorphic behavior: the filaments are straight, and the subunit lattice at radius 4.5 nm is of Lt-type, with left-handed twist and subunits in the short state [22]. (But note that subunits without the inner region can polymerize to form helical filaments if there is a wild-type helical seed [23]).

Since flagellin tends to self-assemble into filaments, it is difficult to crystallize. By clipping off some of the residues at either end of a flagellin chain, Samatey et al. crystallized the F41 fragment of flagellin from the R-type filament of *S. typhimurium*, allowing 2.0 Å resolution of the subunit structure by x-ray scattering [24]. The crystals consist of an anti-parallel arrangement of R-type protofilaments. The lateral interactions normally present in an intact filament are different in the crystal, but the protofilament is still stable. Therefore, the authors of [24] suggested that the protofilament is an "independent, cooperatively switching unit." The structure of the intact R-type filament was revealed at the 4 Å resolution level by electron cryomicroscopy [25]. This work showed that each subunit interacts with its neighbors in the outer core along the 5-, 11-, and 16-start directions, but not along the 6-start direction. In the inner core, each subunit contacts its neighbors along the 5-, 6-, and 11-start directions.

### B. Models

The first quantitative theory of polymorphism in flagella is due to Calladine, who modeled an element of a filament as two rigid discs connected by eleven linear springs [26, 27, 28]. Following Asakura, he supposed that the springs could have one of two rest lengths, with the same spring constant in either case. If all the springs have the same rest length, then a stack of elements would be straight. If some are short and the rest are long, then in equilibrium there will be a variation of spring length, causing the discs in an element to incline relative to each other. A stack of these elements will form a curved filament in equilibrium, with the curvature varying sinusoidally with the number of long springs [27].

Calladine further supposed that the straight state with long springs has the twist of the L-state, the straight state with short springs has the twist of the R-state, and a filament with a mix of short and long springs has a twist that linearly interpolates between the two extremes. These assumptions lead to ten discrete helical states with curvature varying sinusoidally with twist. A key assumption of this model is that the torsion of a helical state is equal to the twist of the elements. Calladine's model was studied further by Hasegawa et al. [29], who used more accurate data to determine the twist parameters of the model, and who also calculated the range of deviations in subunit spacing in single filament of a given helical shape. The predictions of Calladine's model for the possible ground states of flagellar filaments agree reasonably well with measurements of the filament shape [15].

Goldstein et al. used a different approach to model flagellar filaments [30]. They presented a continuum theory for an elastic rod with a preferred direction of curvature, a preferred magnitude of curvature, and a double-well potential for twist. Although the preferred direction of curvature is hard to reconcile with the fact that the flagellin subunits are identical, this model is probably the simplest continuum model for bistable helices. Unlike the model of [26, 27, 28], it provides a framework for calculating the deformation of the filament in response to external forces and moments, such as hydrodynamic loading [31]. This continuum model, along with resistive force theory for hydrodynamic drag, leads to a prediction for the velocity of the front propagating along a helix during a transition from one polymorphic form to another [31].

In this article we develop a new model which has elements similar to both the spring model and the continuum bistable helix model [14]. Like the model of Goldstein and collaborators, our model is a continuum rod theory that predicts the deformation in response to load. Like Calladine's model, our model is based on the two conformations of the protein subunits. However, our model introduces important new features. For example, it does not single out a preferred direction of curvature, but instead assigns every protofilament the same double-well potential for stretch. The model incorporates prestress by assuming there is an elastic mismatch between the inner and outer cores of the filament; this elastic mismatch is necessary to make the absolute minimum of the elastic energy helical instead of straight. Finally, we explicitly treat the cooperative interactions between neighboring subunits. These cooperative interactions are required to make the ground state unique.

## III. FILAMENT ELASTIC ENERGY

The goal of this article is to explain why flagellar filaments are helical and why they undergo polymorphic transformations. Since the characteristic length scale of the helical polymorphs is a micron, much larger than the 5 nm scale of the flagellin subunits, it is natural to formulate a coarse-grained or continuum theory for polymorphism. We model the filament as two concentric elastic cylinders (Fig. 2). The inner cylinder corresponds to the inner core of the filament, and is treated as an elastic rod with a resistance to stretching. The outer cylinder corresponds to the outer core of the filament, and consists of eleven strands which gently wind around the inner core (Fig. 2). Each strand corresponds to a protofilament, although strictly speaking, a protofilament in a flagellar filament includes material from both the inner and outer cores. We divide the outer core into protofilaments but treat the inner core as a single elastic element since only the outer core is implicated in switching between polymorphic forms [21].

Our model treats the eleven strands and the inner core as continua. To define the strains of the strands and the inner core, we choose a reference configuration and label

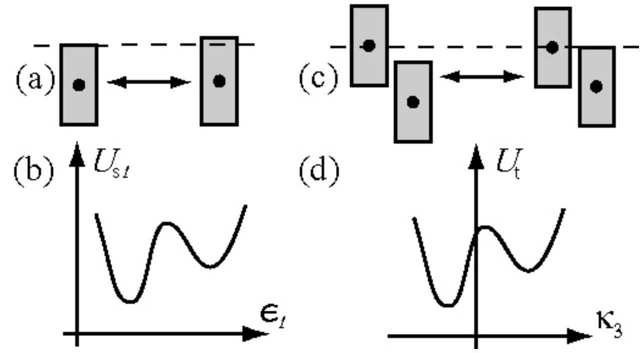

FIG. 3: (a) The two preferred conformations of the subunit. (b) Sketch of double-well potential for stretching a protofilament, with minima corresponding to the two preferred states of (a). (c) The two preferred relative positions of neighboring subunits. (d) Sketch of double-well potential for twist $\kappa_3$.

the points along the inner core with arclength $S$ in the reference configuration. The strain of the inner core is $\epsilon = \mathrm{d}s/\mathrm{d}S - 1$, where $s$ is the actual arclength of the inner core. Note that the strain need not vanish when the inner core is in the reference configuration. Since the difference in subunit spacing of L- and R-type is about 2% of the subunit size, we assume $\epsilon \ll 1$. To define the strain $\epsilon_i$ of the $i$th strand, where $i = 1, 2, \ldots, 11$, consider the cross-section of the filament at $S$. A point on a strand that intersects this cross-section is assigned the label $S$. Thus, if $\mathrm{d}\ell_i$ is the element of length of the $i$th strand, then $\epsilon_i = \mathrm{d}\ell_i/\mathrm{d}S - 1$.

Our model treats the inner core as a rod with a quadratic strain energy per unit length,

$$U_0 = \frac{1}{2}k_\mathrm{s}(\epsilon - \epsilon_0)^2, \tag{1}$$

where $k_\mathrm{s}$ is an elastic constant and $\epsilon_0$ is the strain of the inner core in its unstressed state. The total stretching energy of the inner core is $\int U_0(S)\,\mathrm{d}S$. But since $\mathrm{d}S = \mathrm{d}s/(1+\epsilon) \approx \mathrm{d}s$ to an excellent approximation, we may approximate all energies as integrals over $s$ rather than $S$. The distinction between $s$ and $S$ must be maintained only when computing strain $\epsilon$.

Motivated by the discussion of two preferred subunit conformations, we introduce a "switch" for protofilament extension by defining the stretching energy per unit length of a strand as a double-well potential,

$$U_{\mathrm{s}i} = u\left[(\epsilon_i^2 - \epsilon_\mathrm{p}^2)^2/4 - u_1\epsilon_\mathrm{p}^3\epsilon_i\right], \tag{2}$$

where $u$ is an elastic constant, $\epsilon_\mathrm{p}$ determines the positions of the local minima of $U_{\mathrm{s}i}$ that correspond to the two conformations, and the dimensionless parameter $u_1$ determines the degree of asymmetry of $U_{\mathrm{s}i}$ [Fig. 3(a), (b)]. A term proportional to $\epsilon_i^3$ is disregarded for simplicity.

Since radial spokes connect the inner and outer cores, the strains $\epsilon$ and $\epsilon_i$ are not independent. For example, when the filament is straight, $\epsilon = \epsilon_i$. Mismatch strain arises because the preferred strain of the inner core need not agree with the either of the strains corresponding to the minima of $U_{\mathrm{s}i}$. We will vary the mismatch strain by changing $\epsilon_0$ and keeping $U_{\mathrm{s}i}$ fixed. Mismatch strain is a natural assumption since during self-assembly, the subunits must denature as they travel up the narrow channel at the core of a filament before inserting into their final destination at the distal end [10].

When the filament is curved, the extensions $\epsilon_i$ depend on $i$. To determine this dependence, we follow Calladine and make the simplest assumption by supposing that planar cross-sections of the filament remain planar under bending and twisting [27]. We further suppose that the rod is unshearable. Thus the position of a material point on the $i$th strand at radius $a$ is

$$\mathbf{r}_i = \mathbf{r}_\mathrm{c} + a\cos\beta_i\hat{\mathbf{e}}_1 + a\sin\beta_i\hat{\mathbf{e}}_2, \tag{3}$$

where $\mathbf{r}_\mathrm{c}$ is the position of the centerline of the inner core, $\beta_i = 2\pi(i-1)/11$, and $\hat{\mathbf{e}}_1$ and $\hat{\mathbf{e}}_2$ are orthonormal material frame vectors which are perpendicular to the tangent vector $\hat{\mathbf{e}}_3 = \mathrm{d}\mathbf{r}_c/\mathrm{d}s$ (Fig. 2). Without loss of generality we have chosen $\hat{\mathbf{e}}_1$ to point to the protofilament with $i = 1$.

In this article we choose $a = 4.5\,\mathrm{nm}$, the radius at which the lattice structures of Fig. 1 are reported. Since $\{\hat{\mathbf{e}}_1, \hat{\mathbf{e}}_2, \hat{\mathbf{e}}_3\}$ form an orthonormal frame,

$$\frac{\mathrm{d}\hat{\mathbf{e}}_\mu}{\mathrm{d}s} = \boldsymbol{\kappa} \times \hat{\mathbf{e}}_\mu, \tag{4}$$

where $\boldsymbol{\kappa} = \kappa_\mu\hat{\mathbf{e}}_\mu$, $\kappa_1$ and $\kappa_2$ are the components of the curvature vector $\boldsymbol{\kappa}_\perp = \mathrm{d}\hat{\mathbf{e}}_3/\mathrm{d}s = \kappa_2\hat{\mathbf{e}}_1 - \kappa_1\hat{\mathbf{e}}_2$, and $\kappa_3$ is the twist. The components $\kappa_1$ and $\kappa_2$ are the rates that the orthonormal frame rotates about $\hat{\mathbf{e}}_1$ and $\hat{\mathbf{e}}_2$, respectively. Likewise, the twist $\kappa_3$ is the rate that the orthonormal frame rotates about $\hat{\mathbf{e}}_3$. Note again that since $\epsilon \ll 1$, whether we use $\mathrm{d}/\mathrm{d}s$ or $\mathrm{d}/\mathrm{d}S$ to define $\boldsymbol{\kappa}$ is immaterial. The magnitudes of the components of $\boldsymbol{\kappa}$ are much smaller than $1/a$: $|\kappa_\mu|a \ll 1$. Thus, the relations (3) and (4) together with $\mathrm{d}\ell_i = (\mathrm{d}\mathbf{r}_i/\mathrm{d}S \cdot \mathrm{d}\mathbf{r}_i/\mathrm{d}S)^{1/2}\mathrm{d}S$ imply

$$\epsilon_i = \frac{\mathrm{d}\ell_i - \mathrm{d}S}{\mathrm{d}S} \approx \epsilon + a\kappa_1\sin\beta_i - a\kappa_2\cos\beta_i. \tag{5}$$

Although the strain energy of Eq. (2) involves terms of up to fourth order in $\epsilon_i$, the form of the coefficients of the quartic potential justifies approximating $\epsilon_i$ to first order in $\epsilon$ and $\kappa_\mu a$.

Note that the twist $\kappa_3$ does not appear to first order since the protofilaments are almost longitudinal. For example, at radius 4.5 nm, the angle between a protofilament and the longitude is $-1.45^\circ = -0.0253\,\mathrm{rad}$ in L-type and $3.46^\circ = 0.0605\,\mathrm{rad}$ in R-type [15].

The stretching energy of all the strands is $U_\mathrm{s} = \Sigma_{i=1}^{11}U_{\mathrm{s}i}$, or

$$\frac{U_\mathrm{s}}{11} = \frac{u}{4}\left[(\epsilon^2 - \epsilon_\mathrm{p}^2)^2 + (3\epsilon^2 - \epsilon_\mathrm{p}^2)a^2\kappa^2 + \frac{3}{8}a^4\kappa^4\right] - u_1\epsilon_\mathrm{p}^3\epsilon \tag{6}$$

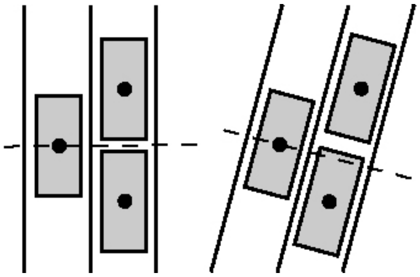

FIG. 4: Illustration of how twist causes neighboring subunits to slide past each other. The subunits rotate rigidly but the lattice of centers of mass shears. The angle of shear has been exaggerated for illustration.

where $\kappa = |\boldsymbol{\kappa}_\perp| > 0$ is the curvature of the filament. Although $U_{\mathrm{s}i}$ has a term linear in $\epsilon_i$, there are only even powers of $\kappa$ in $U_{\mathrm{s}}$. Thus, the energy $U_{\mathrm{s}}$ depends on the magnitude of the curvature. There is no natural (or spontaneous) *direction* of curvature since all subunits are identical. However, the subunits may be in different states. For example, if $3\epsilon^2 - \epsilon_{\mathrm{p}}^2 < 0$, then there will be a natural *magnitude* of curvature, and a distribution of subunit states around the circumference of the filament. In this case, the direction of the curvature vector at a point $s$ may point in any direction in the plane of the cross-section. Note also that $U_{\mathrm{s}}$ shows no trace of the original eleven-fold symmetry of the sum of $U_{\mathrm{s}i}$ over the eleven protofilaments; the resistance to bending is isotropic for a rod with a cross-section with a symmetry greater than two-fold [32]. This isotropy rules out couplings between twist and curvature like those that arise in the mechanics of DNA [33].

In our model, lateral interactions between neighboring subunits on different protofilaments lead to a resistance to twist. We follow the suggestion of Namba and Vonderviszt [34] and suppose that neighboring protofilaments have two preferred relative displacements along the local protofilament direction [Fig. 3(c), (d)]. These interactions are at the quaternary level; they do not require a conformational change of the subunit. As Fig. 4 illustrates, twisting a filament causes neighboring protofilaments to slide past each other. Therefore, two preferred relative displacements are equivalent to two preferred twists. Thus, we introduce a second switch, a double-well potential for twist:

$$U_{\mathrm{t}} = v\left[\frac{1}{4}a^4(\kappa_3^2 - \Omega_{\mathrm{p}}^2)^2 - \bar{v}_1 a^4 \Omega_{\mathrm{p}}^3 \kappa_3\right], \qquad (7)$$

where $v$ is an elastic constant, $\Omega_{\mathrm{p}}$ determines the two preferred twists, and $\bar{v}_1$ makes the potential asymmetric. As for our potential for extension, Eq. (2), a cubic term is disregarded for simplicity.

In addition to the switches for extension and twist, the filament structure suggests a coupling between twisting and stretching. As mentioned earlier, the electron cryomicroscopy studies of the intact R-type filament show that each subunit has contacts with its neighbors along the 5-, 11-, and 16-start directions in the outer core. Our model effectively replaces all the inner core lattice contacts with the inner tube, and those along the 11-start direction of the outer tube by a double-well potential. Since the 16-start direction is almost longitudinal, like the 11-start direction, we ignore it for simplicity. The 5-start helices make an angle of approximately −45° with the longitude in both the straight filaments. This contact will lead to twist resistance, as well as a coupling between twist and stretch. To understand the sign of this coupling, consider a straight R-type filament in the limit where the bonds along the 5-start direction are rigid and unable to stretch. Pulling on the filament will cause the left-handed 5-start helices to untwist a little, leading to an increase in $\kappa_3$, the twist of the 11-start helices. Likewise, an applied moment which tends to unwind the 5-start helices will cause the filament to lengthen. Thus, the twist stretch coupling is of the form

$$U_5 = -k_5 a \epsilon \kappa_3, \qquad (8)$$

where $k_5$ is a positive elastic constant.

The 5- and 6-start contacts in the inner core will also contribute to the twist-stretch coupling. Without knowing the relative strength of these bonds, we cannot predict the sign of the contribution to the twist-stretch coupling, since the 5-start helices are left-handed and the 6-start helices are right-handed. However, since the outer core bonds lie at a radius roughly double that of the inner core bonds, and bending and twisting moduli in rod theory scale as the third power of radius for a hollow rod [32], we assume that the contribution to the elastic energy of the inner core bonds is dominated by that of the outer core bonds. Note also that the 5-start bonds will contribute to the bending and twisting resistance of the filament; these effects are already accounted for in the bending terms of $U_{\mathrm{s}}$ and the twist potential $U_{\mathrm{t}}$. Also, since the high-resolution structure of the intact L-type filament is currently unavailable, we make the simplest assumption and suppose there are contacts along the 5-start direction but not the 6-start direction in L-type as well as R-type. Finally, we note that there could be a twist-stretch coupling arising from the elasticity of the subunit itself. For example, pulling on a subunit along the 11-start direction could cause it to shear as well as stretch, causing the whole filament to twist in a right or left-handed sense. We know of no evidence for or against this possibility, but we must acknowledge that our choice of the sign of $k_5$ is provisional.

The terms of the elastic energy introduced above ($U_{\mathrm{s}}$, $U_{\mathrm{t}}$, and $U_5$) determine the extension $\epsilon$, the curvature $\kappa$, and the twist $\kappa_3$. However, these variables do not completely determine the shape of the filament: two rods may have the same curvature and the same twist, but different shapes. For example, Fig. 5 shows circular and helical filaments that have the same curvature and the same twist, and hence the same value of $U_{\mathrm{s}} + U_{\mathrm{t}} + U_5$ (assuming $\epsilon$ is the same for both filaments). To see what kind of term is required to remove this degeneracy, consider the special

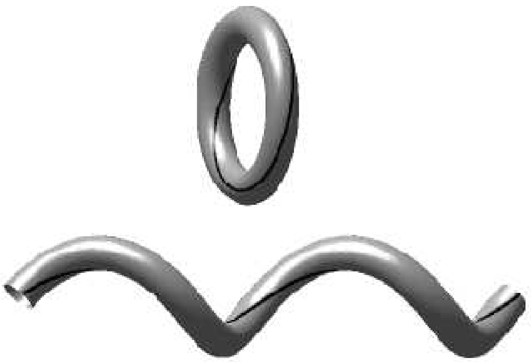

FIG. 5: Two rods with the same curvature and the same twist. The black line traces the path of the head of the vector $\hat{\mathbf{e}}_1$. The circular rod is twisted through one turn to make $\kappa_3 = 1/R_{\rm c}$, where $R_{\rm c} = 1/\kappa$ is the radius of the circle.

case of a rod bent into a circle. In Fig. 5, the curvature vector of the circle lies in the plane of the circle, pointing toward the center. Since the twist is nonzero, $\kappa_3 \neq 0$, the components of the curvature vector in the material frame depend on arclength, $\mathrm{d}\kappa_{1,2}/\mathrm{d}s \neq 0$. Therefore, by Eq. (5), the extension $\epsilon_i$ of the $i$th protofilament also depends on arclength. Contrast this example with the case of a circular rod with no twist, $\kappa_3 = 0$. In this case, $\kappa_1 = 0$ and $\kappa_2 = 1/R$, and the extension $\epsilon_i$ of each protofilament is uniform. The shortest protofilament lies a circle of radius $R - a$, and the longest protofilaments each lie on a circle with radius slightly less than $R + a$ (since there is an odd number of protofilaments). The helix in Fig. 5 is analogous to the circle with no twist; the pitch and radius have been carefully chosen to ensure that $\epsilon_i$ is uniform.

Motivated by these observations, we suppose there is an energy penalty when neighboring subunits on the same protofilament are in different states. This cooperative interaction is implicit in the assumptions of Asakura [6] and Calladine [26], who supposed all subunits in a given protofilament prefer to be in the same state. Also, as mentioned in section II A, the integrity of the protofilaments in crystallized R-type subunits led Samatey and collaborators to suppose there are strong cooperative interactions along the 11-start direction [24]. In our continuum model, the cooperative energy penalizes nonuniform extension of each protofilament:

$$U_{\rm c} = \frac{wa}{2}\sum_{i=1}^{11}\left(\frac{\mathrm{d}\epsilon_i}{\mathrm{d}s}\right)^2, \tag{9}$$

where $w$ is an elastic constant with units of energy per unit length. The cooperative interaction Eq. (9) stabilizes the state of a given subunit, depending on the state of the subunits neighbors, in accord with the concept of conformational spread [4]. In terms of the filament variables $\epsilon$, $\kappa_1$, and $\kappa_2$, the cooperative interaction is

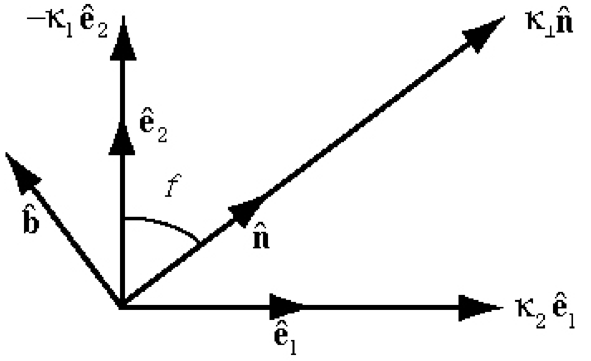

$-\kappa_1\,\hat{\mathbf{e}}_2$
$\kappa_\perp\hat{\mathbf{n}}$
$\hat{\mathbf{e}}_2$
$f$
$\hat{\mathbf{b}}$
$\hat{\mathbf{n}}$
$\kappa_2\,\hat{\mathbf{e}}_1$
$\hat{\mathbf{e}}_1$

FIG. 6: The basis vectors of the material and Serret-Frenet frames in the plane of the rod cross-section.

$$U_{\rm c} = \frac{11wa}{2}\left[\left(\frac{\mathrm{d}\epsilon}{\mathrm{d}s}\right)^2 + \frac{a^2}{2}\left(\frac{\mathrm{d}\kappa_1}{\mathrm{d}s}\right)^2 + \frac{a^2}{2}\left(\frac{\mathrm{d}\kappa_2}{\mathrm{d}s}\right)^2\right]. \tag{10}$$

It is also convenient to write $U_{\rm c}$ in terms of the Serret-Frenet basis [35]. Recall that the Serret-Frenet basis of a space curve is an orthonormal frame consisting of the tangent $\hat{\mathbf{t}} = \hat{\mathbf{e}}_3 = \mathrm{d}\mathbf{r}/\mathrm{d}s$, normal $\hat{\mathbf{n}}$, and binormal $\hat{\mathbf{b}}$, where

$$\frac{\mathrm{d}}{\mathrm{d}s}\begin{pmatrix}\hat{\mathbf{n}}\\ \hat{\mathbf{b}}\\ \hat{\mathbf{t}}\end{pmatrix} = \begin{pmatrix}0 & \tau & -\kappa\\ -\tau & 0 & 0\\ \kappa & 0 & 0\end{pmatrix}\begin{pmatrix}\hat{\mathbf{n}}\\ \hat{\mathbf{b}}\\ \hat{\mathbf{t}}\end{pmatrix}, \tag{11}$$

and $\tau$ is the torsion. (Recall also that unlike $\tau$, $\kappa_1$, $\kappa_2$, and $\kappa_3$, each of which may have either sign, the curvature $\kappa$ is nonnegative.) Since $\{\hat{\mathbf{n}}, \hat{\mathbf{b}}\}$ and $\{\hat{\mathbf{e}}_1, \hat{\mathbf{e}}_2\}$ span the same plane, they are related by a rotation:

$$\hat{\mathbf{e}}_1 = \sin f\,\hat{\mathbf{n}} - \cos f\,\hat{\mathbf{b}} \tag{12}$$

$$\hat{\mathbf{e}}_2 = \cos f\,\hat{\mathbf{n}} + \sin f\,\hat{\mathbf{b}}. \tag{13}$$

These relations, together with $\boldsymbol{\kappa}_\perp = \mathrm{d}\hat{\mathbf{e}}_3/\mathrm{d}s$, imply $\kappa_1 = -\kappa\cos f$ and $\kappa_2 = \kappa\sin f$ (see Fig. 6). The relation between twist and torsion may be found by writing $\kappa_3 = -\hat{\mathbf{e}}_1\cdot\mathrm{d}\hat{\mathbf{e}}_2/\mathrm{d}s$ in terms of the Serret-Frenet basis:

$$\kappa_3 = \mathrm{d}f/\mathrm{d}s + \tau. \tag{14}$$

Thus,

$$U_{\rm c} = \frac{11wa}{2}\left[\left(\frac{\mathrm{d}\epsilon}{\mathrm{d}s}\right)^2 + \frac{a^2}{2}\left(\frac{\mathrm{d}\kappa}{\mathrm{d}s}\right)^2 + \frac{a^2}{2}\left(\tau - \kappa_3\right)^2\right]. \tag{15}$$

The cooperative term $U_{\rm c}$ is at its absolute minimum when the extension and curvature of the filament are uniform, and when the torsion is equal to the twist. Thus, $U_{\rm c}$ removes the degeneracy in the filament ground states. When $\tau = \kappa_3$ [as for the helix of Fig. 5, with radius $R = \kappa/(\kappa^2 + \kappa_3^2)$ and pitch $P = 2\pi\kappa_3/(\kappa^2 + \kappa_3^2)$], the angle

$f$ is constant, and therefore the Serret-Frenet frame does not rotate relative to the material frame as $s$ changes. Without loss of generality we may consider $f = \pi/2$, in which case the Serret-Frenet frame and the material frame align for all $s$. Therefore, the protofilament $i = 1$ traces out the path $\mathbf{r}(s)+a\mathbf{n}(s)$; this path is the "shortest path" on the surface of the helical filament, analogous to the path of radius $R-a$ on the surface of a circular tube with centerline radius $R$ and tube radius $a$.

To summarize, the total elastic energy is

$$E = \int (U_0 + U_\mathrm{s} + U_\mathrm{t} + U_5 + U_\mathrm{c})\mathrm{d}s. \qquad (16)$$

The material parameters, such as $\epsilon_0$ and $\bar{v}_1$, for example, are functions of environmental conditions such as pH and temperature. These functions must be determined by a microscopic theory and are therefore outside the scope of our coarse-grained theory. Therefore, in the following sections we will determine the filament shape as a function of the material parameters and externally imposed moments and forces.

## IV. SIMPLE MODEL: STIFF CENTRAL SPRING

First we consider the simplified model studied in [14], in which the stretching stiffness of the inner core is large ($k_\mathrm{s}/u \to \infty$), the nonlinear stretching potential is symmetric ($u_1 = 0$), and the twist-stretch coupling is disregarded ($k_5 = 0$). Since the central core is so stiff, the extension of the filament is $\epsilon = \epsilon_0$, and the total energy density (up to an unimportant additive constant) simplifies to

$$\begin{aligned} U &= \frac{\tilde{u}}{4} a^4 \left(\kappa^2 - \kappa_0^2\right)^2 \\ &+ v \left[\frac{a^4}{4}\left(\kappa_3^2 - \Omega_\mathrm{p}^2\right)^2 - \bar{v}_1 a^4 \Omega_\mathrm{p}^3 \kappa_3\right] \\ &+ \frac{11 w a^3}{4}\left[\left(\frac{\mathrm{d}\kappa_1}{\mathrm{d}s}\right)^2 + \left(\frac{\mathrm{d}\kappa_2}{\mathrm{d}s}\right)^2\right], \end{aligned} \qquad (17)$$

where $\tilde{u} = 33u/8$ and $\kappa_0^2 a^2 = 4(\epsilon_\mathrm{p}^2 - 3\epsilon_0^2)/3$. Note that since $k_\mathrm{s}/u \to \infty$, the effect of making $k_5$ nonzero may be captured by shifting the value of $\bar{v}_1$ in the model with $k_5 = 0$.

### A. Ground states

To find the configuration of the filament, we minimize the energy $\int U \mathrm{d}s$ by varying $\kappa_1$, $\kappa_2$, and $\kappa_3$. In this subsection, we find the configuration in the absence of external moments and forces and as a function of the material parameters. In our discussion we will only consider straight and helical filaments. The cooperative term has an absolute minimum for constant $\kappa_1$ and $\kappa_2$; therefore, as discussed above we take $f = \pi/2$, or $\kappa_1 = 0$. Minimizing $U$ over $\kappa_2$ leads to

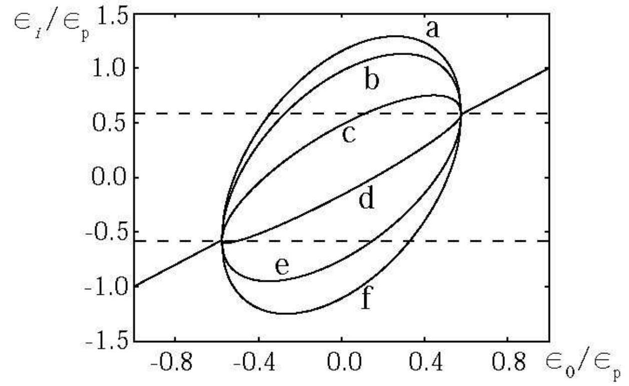

FIG. 7: Protofilament extension $\epsilon_i$ vs. preferred extension $\epsilon_0$ of the inner core for $i = 1$ (a), $i = 2$ and $i = 11$ (b), $i = 3$ and $i = 10$ (c), $i = 4$ and $i = 9$ (d), $i = 5$ and $i = 8$ (e), $i = 6$ and $i = 7$ (f). The region between the horizontal dashed lines is the unstable region.

$$\kappa_2 = 0 \qquad (18)$$

for $|\epsilon_0| > \epsilon_\mathrm{p}/\sqrt{3}$ (or $\kappa_0^2 < 0$), and

$$\kappa_2^2 a^2 = 4(\epsilon_\mathrm{p}^2 - 3\epsilon_0^2)/3 \qquad (19)$$

for $|\epsilon_0| < \epsilon_\mathrm{p}/\sqrt{3}$ (or $\kappa_0^2 > 0$).

To interpret these results physically, consider a straight filament. If $|\epsilon_0| < \epsilon_\mathrm{p}/\sqrt{3}$, then the strain $\epsilon_i$ of each of the eleven protofilaments lies in the unstable region of the double-well potential, where $\partial^2 U_\mathrm{s}/\partial\epsilon^2 < 0$. Therefore, the straight state is unstable. The filament can lower its energy by bending, since in the bent state, the protofilaments on the inside of the curve will have an extension close to $-\epsilon_\mathrm{p}$, and the protofilaments on the outside of the curve will have an extension close to $\epsilon_\mathrm{p}$. Figure 7 shows the stretch $\epsilon_i = \epsilon_0 + (4/3)^{1/2}\sqrt{\epsilon_\mathrm{p}^2 - 3\epsilon_0^2}\cos[2\pi(i-1)/11]$ of the individual protofilaments as a function of $\epsilon_0$. Note that when the filament is bent, there are always some protofilaments with an unstable extension $|\epsilon_i| < \sqrt{3}\epsilon_\mathrm{p}$, even though the filament as a whole is stable.

This last observation illustrates the importance of the central stretching potential, Eq. (1). If there were no central core, then $k_\mathrm{s} = 0$, as in the models of [26] and [29]. When $k_\mathrm{s} = 0$ in our model, both $\epsilon$ and $\kappa_2$ are determined by minimizing $U_0 + U_\mathrm{s}$. States with $\kappa_2 \neq 0$ are still possible, despite the absence of lattice mismatch, but straight states always have lower energy. This metastability of curved states when $k_\mathrm{s} = 0$ is consistent with the experimental observation that filaments formed from subunits with truncated ends are straight, unless the subunits grow on a helical seed filament [23]. The cooperative interactions at the junction between the seed filament and the filament consisting of truncated subunits can favor curvature.

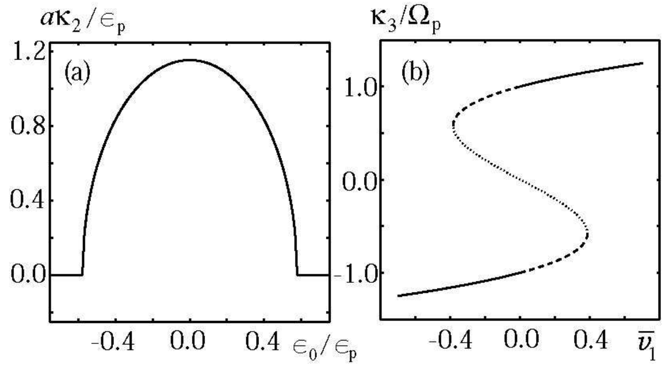

FIG. 8: (a) Curvature vs. $\epsilon_0$ and (b) twist vs. $\bar{v}_1$ for the simple model of Section IV. In (b), the solid lines correspond to the states of lowest energy, the dashed lines to metastable states, and the dotted line to unstable states.

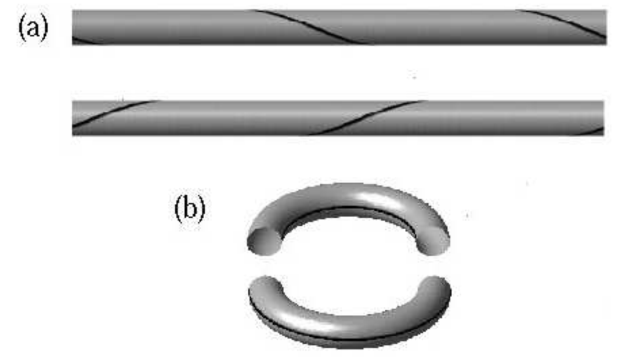

FIG. 9: (a) Applying twisting moments to the right-handed rod (top) causes it to snap through to a left-handed state (bottom). (b) The rod on top has $\kappa_2 > 0$; the rod on the bottom has $\kappa_2 < 0$. Applying moments as shown to the top rod causes it to snap through.

The twist is determined by minimizing $U$ over $\kappa_3$, which yields

$$\kappa_3^3 - \Omega_p^2 \kappa_3 = \bar{v}_1 \Omega_p^3. \tag{20}$$

When $\bar{v}_1^2 > 4/27$, there is only one value of $\kappa_3$ that solves Eq. (20). This solution is stable since $\partial^2 U/\partial\kappa_3^2 > 0$. When $\bar{v}_1^2 < 4/27$, there are three solutions. One of these solutions has $\partial^2 U/\partial\kappa_3^2 < 0$, and is unstable. Of the two stable solutions, the one with the same sign as $\bar{v}_1$ has lower energy.

Figure 8(a) shows the dependence of curvature $\kappa_2$ on the preferred stretch $\epsilon_0$ of the central potential, and Fig. 8(b) shows the dependence of twist $\kappa_3$ on the asymmetry parameter $\bar{v}_1$. These figures directly show the continuous nature of the transition from straight to bent, and the discontinuous nature of the transition from left- to right-handed. Note that since $\epsilon_0$ and $\bar{v}_1$ are independent parameters, the stretch and the twist are not coupled in our simple model.

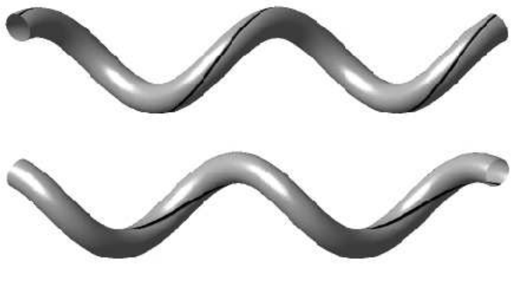

FIG. 10: Two helical filaments. The black line traces along the path of the protofilament $i = 1$. Top: a filament with $\kappa_2 < 0$ and $\kappa_3 < 0$. Applying axial moments of sufficient magnitude in the directions shown causes the filament to snap through to a state with $\kappa_2 > 0$ and $\kappa_3 > 0$ (bottom).

### B. Response to external moment

The goal of this subsection is to calculate $\boldsymbol{\kappa}$ for a filament subject to an external moment $\mathbf{M} = M\hat{\mathbf{z}}$, where the $z$-axis is along the helical axis for helices and along the tangent vector for straight filaments. We begin with a qualitative discussion. Consider a straight filament with a double-well potential for twist and a single well potential for curvature [for example, a filament with $\kappa_0^2 < 0$; see Eq. (17)]. To simplify the discussion, take the twist potential to be symmetric: $\bar{v}_1 = 0$. Suppose the filament is in a state of right-handed twist when $M = 0$. Applying a positive twisting moment will tend to increase the twist of the filament. As the positive moment increases, the twist of the filament will increase continuously. Applying a negative moment to the filament will tend to untwist it [Fig. 9(a), top]. As the magnitude of the negative moment increases, the filament will untwist continuously until it snaps through to a left-handed twist at a critical moment. Further increase in the magnitude of the moment will cause the left-handed twist to increase continuously. Once the moment is released, the filament will remain in a left-handed state [see Fig. 9(a), bottom]. This state is the same energy as the right-handed state when $\bar{v}_1 = 0$ (and $k_5 = 0$); when $\bar{v}_1 > 0$, this state is metastable.

The situation is similar for a filament with a double-well potential for curvature and a single well potential for twist (for example, a filament with $\kappa_0^2 > 0$ and $\Omega_p^2 < 0$). In the absence of external moment, the shape of this filament will be an arc of a circle. Suppose $\kappa_2 > 0$; that is, the material frame vector $\hat{\mathbf{e}}_1$ points to the center of curvature, or equivalently, the protofilament with $i = 1$ lies on the inside of the curved surface [Fig. 9(b), top]. Applying bending moments with sufficient magnitudes causes the filament to snap through to a state of negative $\kappa_2$. When the bending moments are released, the filament remains in a state of $\kappa_2 < 0$.

A helical filament with double-well potentials for curvature and twist has snap-through behavior in both the curvature and twist, since a moment $M$ along the helical axis may be resolved into a twisting moment $M_\mathrm{t}$ along the filament tangent vector and a bending moment $M_\mathrm{b}$ perpendicular to the filament tangent vector. Figure 10 shows helical states analogous to those of Fig. 9(a) and (b).

We now turn to the quantitative determination of the response to an external moment. The variables $\kappa_\mu$ used in the calculation of the phase diagram are intrinsic; that is, they depend on the shape but not the orientation of the filament. Since an external moment specifies a direction in space, it is convenient to use extrinsic variables such as the Euler angles, which are defined using a space-fixed frame. We will use the convention of Love [36]. The material frame at $s$ is generated by first rotating the frame $\{\hat{\mathbf{x}}, \hat{\mathbf{y}}, \hat{\mathbf{z}}\}$ about $\hat{\mathbf{z}}$ through an angle $\psi$ to obtain the frame $\hat{\mathbf{e}}_i'$, then by rotating this frame about $\hat{\mathbf{e}}_2'$ by $\theta$ to obtain the frame $\hat{\mathbf{e}}_i''$, and finally by rotating the frame $\hat{\mathbf{e}}_i''$ by $\phi$ about $\hat{\mathbf{e}}_3''$ to obtain $\hat{\mathbf{e}}_i$ [see Eqs. (A1)–(A9) in Appendix A]. Our convention is to have the Euler angles lie in the ranges

$$\begin{aligned} 0 &\leq \psi < 2\pi && (21)\\ -\pi/2 &\leq \theta \leq \pi/2 && (22)\\ 0 &\leq \phi < 2\pi, && (23) \end{aligned}$$

so that the component of $\hat{\mathbf{e}}_3$ along $\hat{\mathbf{z}}$ is always nonnegative. The formulas for the material frame vectors in terms of Euler angles are given in Eqs. (A7–A9). To determine the components of the vector $\boldsymbol{\kappa}$ in terms of Euler angles, rewrite Eq. (4) as $\kappa_\mu = \epsilon_{\mu\nu\lambda} \mathrm{d}\hat{\mathbf{e}}_\nu/\mathrm{d}s \cdot \hat{\mathbf{e}}_\lambda$, where $\epsilon_{ijk}$ is the Levi-Civita symbol, and find

$$\begin{aligned} \kappa_1 &= \dot{\theta}\sin\phi - \dot{\psi}\sin\theta\cos\phi && (24)\\ \kappa_2 &= \dot{\theta}\cos\phi + \dot{\psi}\sin\theta\sin\phi && (25)\\ \kappa_3 &= \dot{\phi} + \dot{\psi}\cos\theta, && (26) \end{aligned}$$

where the dot signifies differentiation with respect to $s$; for example, $\dot{\theta} = \mathrm{d}\theta/\mathrm{d}s$.

In equilibrium, equal and opposite moments must be applied to the ends of the rod. The principle of virtual work is therefore

$$\delta E - \mathbf{M} \cdot [\delta\boldsymbol{\Upsilon}(L) - \delta\boldsymbol{\Upsilon}(0)] = 0, \tag{27}$$

where $\delta\Upsilon_\mu(s)$ is the angle of the virtual rotation of the material frame about $\hat{\mathbf{e}}_\mu$. For example, the angle of a virtual rotation of the material frame about $\hat{\mathbf{e}}_3$ is given by the $\hat{\mathbf{e}}_2$ component of the infinitesimal change in $\hat{\mathbf{e}}_1$: $\delta\Upsilon_3 = \hat{\mathbf{e}}_2 \cdot \delta\hat{\mathbf{e}}_1$. The general relation follows by taking cyclic permutations, $\delta\Upsilon_\mu = \epsilon_{\mu\nu\lambda}\delta\hat{\mathrm{e}}_\nu \cdot \hat{\mathrm{e}}_\lambda$. Using Eqs. (A7–A9) to calculate

$$\begin{aligned} \delta\Upsilon_1 &= -\delta\psi\sin\theta\cos\phi + \delta\theta\sin\phi && (28)\\ \delta\Upsilon_2 &= \delta\psi\sin\theta\sin\phi + \delta\theta\cos\phi && (29)\\ \delta\Upsilon_3 &= \delta\psi\cos\theta + \delta\phi && (30) \end{aligned}$$

yields $\mathbf{M} \cdot \delta\boldsymbol{\Upsilon} = M\delta\psi + M\cos\theta\delta\phi$.

Taking the variation of $E = \int U \mathrm{d}s$ with respect to $(\Xi_1, \Xi_2, \Xi_3) = (\psi, \theta, \phi)$ leads to the Euler-Lagrange equations

$$\frac{\partial U}{\partial \Xi_a} - \frac{\mathrm{d}}{\mathrm{d}s}\frac{\partial U}{\partial \dot{\Xi}_a} + \frac{\mathrm{d}^2}{\mathrm{d}s^2}\frac{\partial U}{\partial \ddot{\Xi}_a} = 0, \tag{31}$$

where $a$ runs from 1 to 3. Since $U$ is independent of $\psi$, $\phi$, and $\ddot{\phi}$ (see the appendix), these equations simplify to

$$\begin{aligned} -\frac{\mathrm{d}}{\mathrm{d}s}\frac{\partial U}{\partial \dot{\psi}} + \frac{\mathrm{d}^2}{\mathrm{d}s^2}\frac{\partial U}{\partial \ddot{\psi}} &= 0 && (32)\\ \frac{\partial U}{\partial \theta} - \frac{\mathrm{d}}{\mathrm{d}s}\frac{\partial U}{\partial \dot{\theta}} + \frac{\mathrm{d}^2}{\mathrm{d}s^2}\frac{\partial U}{\partial \ddot{\theta}} &= 0 && (33)\\ -\frac{\mathrm{d}}{\mathrm{d}s}\frac{\partial U}{\partial \dot{\phi}} &= 0 && (34) \end{aligned}$$

To complete the description of the variational problem, we assume natural boundary conditions: $\delta\Xi_a(0)$ and $\delta\Xi_a(L)$ are arbitrary, and $\delta\dot{\Xi}_a(0) = \delta\dot{\Xi}_a(L) = 0$. Noting again that $U$ is independent of $\ddot{\phi}$, we find that these natural boundary conditions imply

$$\begin{aligned} \left[\frac{\partial U}{\partial \ddot{\Xi}_a}\right]_{s=L} &= 0 && (35)\\ \left[\frac{\partial U}{\partial \dot{\psi}} - \frac{\mathrm{d}}{\mathrm{d}s}\frac{\partial U}{\partial \ddot{\psi}}\right]_{s=L} &= M && (36)\\ \left[\frac{\partial U}{\partial \dot{\theta}} - \frac{\mathrm{d}}{\mathrm{d}s}\frac{\partial U}{\partial \ddot{\theta}}\right]_{s=L} &= 0 && (37)\\ \left[\frac{\partial U}{\partial \dot{\phi}}\right]_{s=L} &= M\cos\theta. && (38) \end{aligned}$$

Exactly the same conditions apply at $s = 0$.

The equations (32–38) are derived without making any assumptions on the form of $\psi$, $\theta$, and $\phi$. We now turn to the special cases of straight and helical filaments. A helix has a parameterization

$$\mathbf{r}(s) = \left(\frac{\sin\theta}{\dot{\psi}}\sin(\dot{\psi}s), -\frac{\sin\theta}{\dot{\psi}}\cos(\dot{\psi}s), s\cos\theta\right), \tag{39}$$

with $\dot{\theta} = 0$ and $\ddot{\psi} = 0$. For constant $\theta$ and constant $\dot{\psi}$, Eq. (35) with $a = 2$ (and the corresponding equation at $s = 0$) imply $\partial U/\partial\ddot{\theta} = (11/2)wa^3\dot{\psi}\dot{\phi}\sin\theta = 0$ at $s = L$ and $s = 0$. But $\theta \neq 0$ and $\dot{\psi} \neq 0$ for a helix; therefore $\dot{\phi} = 0$ at the ends of the filament. On the other hand, since $U$ is independent of $\phi$ and $\ddot{\phi}$, Eq. (34) implies

$$\frac{\partial U}{\partial \dot{\phi}} = va^4\left(\dot{\phi} + \dot{\psi}\cos\theta\right)\left[\left(\dot{\phi} + \dot{\psi}\cos\theta\right)^2 - \Omega_\mathrm{p}^2\right] \tag{40}$$

is constant. Since $\dot{\psi}$ and $\theta$ are both constant, $\dot{\phi}$ must be constant. Therefore, $\dot{\phi} = 0$ for all $s$. Note that without the cooperative term, this conclusion would not follow. With loss of generality we choose $\phi = \pi/2$. A shift in $\phi$ amounts to redefining which protofilament has $i = 1$.

In general, the Euler angle $\phi$ differs from the angle $f$ defined in Fig. 6. However, there is a simple relation between $\phi$ and $f$ for a helical rod. To derive this relation, use Eqs. (A4–A6) to show

$$\kappa\hat{\mathbf{n}} = \mathrm{d}\hat{\mathbf{e}}_3''/\mathrm{d}s = \dot{\theta}\hat{\mathbf{e}}_1'' + \dot{\psi}\sin\theta\hat{\mathbf{e}}_2'' \tag{41}$$

Thus, for a helix for which $\dot{\theta} = 0$, the normal is parallel or antiparallel to $\hat{\mathbf{e}}_2''$; $\hat{\mathbf{n}} = \hat{\mathbf{e}}_2''$ and $f = \phi$ when $\kappa_2 > 0$, and $\hat{\mathbf{n}} = -\hat{\mathbf{e}}_2''$ and $f = \phi + \pi$ when $\kappa_2 < 0$. With our choice for $\phi$, $f = \pi/2$ when $\kappa_2 > 0$ and $f = 3\pi/2$ when $\kappa_2 < 0$.

Returning to the Euler-Lagrange equations, we note that Eqs. (34) and (38) imply $\partial U/\partial\dot{\phi} = M\cos\theta$ for all $s$. Likewise, since $\partial U/\partial\ddot{\psi} = 0$ when $\dot{\theta} = \ddot{\psi} = 0$, Eqs. (32) and (36) imply $\partial U/\partial\dot{\psi} = M$ for all $s$. The other Euler-Lagrange equation, Eq. (33) with $\dot{\theta} = \ddot{\psi} = \dot{\phi} = 0$, does not yield an independent equation. Thus,

$$\begin{aligned} \dot{\psi}\sin\theta\left(\dot{\psi}^2\sin^2\theta - \kappa_0^2\right) &= \frac{M}{\tilde{u}a^4}\sin\theta \qquad (42)\\ \dot{\psi}\cos\theta\left(\dot{\psi}^2\cos^2\theta - \Omega_{\mathrm{p}}^2\right) &= \frac{M}{va^4}\cos\theta. \qquad (43)\end{aligned}$$

Note that under the assumption of uniform $\kappa_1$ and $\kappa_2$, Eqs. (42–43) also follow from the constitutive relations

$$M_\mu = \frac{\partial U}{\partial\kappa_\mu}, \tag{44}$$

with $M_1 = 0$, $M_2 = M\sin\theta$, and $M_3 = M\cos\theta$.

First we analyze a rod that is helical when $M = 0$; hence $\kappa_0^2 > 0$, and we may assume $\theta \neq 0$ and $\theta \neq \pi/2$. It is convenient to define $\sigma^2 = \kappa_0^2 + \Omega_{\mathrm{p}}^2$, the pitch angle $\theta_0$ for zero applied moment, $\tan\theta_0 = \kappa_0/\Omega_{\mathrm{p}}$, and the dimensionless moment $m = M(\tilde{u} + v)/(\tilde{u}va^4\sigma^3)$. The angle $\theta$ may be eliminated from Eqs. (42) and (43) to yield a simple cubic equation for $\dot{\psi}$:

$$\dot{\psi}^3/\sigma^3 - \dot{\psi}/\sigma = m. \tag{45}$$

The curve relating $\dot{\psi}/\sigma$ to $m$ is precisely the same as the curve in Fig 8(b). Equation 45 determines the handedness of the filament since $\kappa_3 = \dot{\psi}\cos\theta$, and $\cos\theta > 0$. Combining Eq. (45) with Eq. (42) leads to

$$\sin^2\theta = \frac{v}{\tilde{u} + v} + \left(\sin^2\theta_0 - \frac{v}{\tilde{u} + v}\right)\frac{\sigma^2}{\dot{\psi}^2}. \tag{46}$$

The sign of $\kappa_2 = \dot{\psi}\sin\theta$ is not determined by these equations since Eq. (46) is invariant under $\theta \mapsto -\theta$. The consequence of this invariance is that for every $M$, there are two helical solutions with the same curvature and twist, one with $\kappa_2 < 0$ (as in Fig. 11, top), and one with the $\kappa_2 > 0$ (as in Fig. 11, bottom). This symmetry remains valid in the full model also.

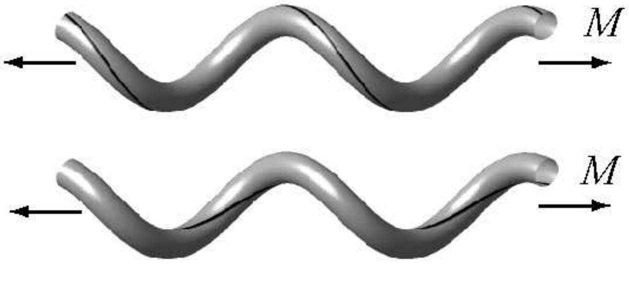

FIG. 11: Two helices with the same curvature and twist, one with $\kappa_2 < 0$ (top), and one with $\kappa_2 > 0$ (bottom). In each case, the black line traces the path of the protofilament $i = 1$.

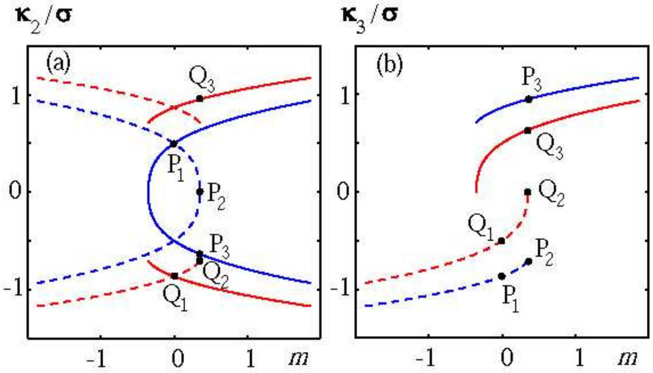

FIG. 12: (a) Signed curvature $\kappa_2$ vs. $m$ for $\tilde{u} = v$ and $\theta_0 = \pi/6$ (blue curves) and $\theta_0 = \pi/3$ (red curves). The dashed lines correspond to left-handed states. (b) Twist $\kappa_3$ vs. $m$ with parameters as in (a).

Under the restrictions of uniform $\dot{\psi}$, uniform $\theta$, and $\phi = \pi/2$, these solutions are stable if and only if the Hessian matrix

$$\mathsf{H} = \begin{bmatrix} \partial^2U/\partial\dot{\psi}^2 & \partial^2U/(\partial\dot{\psi}\partial\theta) \\ \partial^2U/(\partial\theta\partial\dot{\psi}) & \partial^2U/\partial\theta^2 \end{bmatrix} \tag{47}$$

is positive definite, or equivalently, $\mathrm{d}\dot{\psi}/\mathrm{d}M > 0$. To see why these conditions are equivalent, note under the restrictions just mentioned the Euler-Lagrange equations are

$$\begin{aligned} \partial U/\partial\dot{\psi} - M &= 0 \qquad (48)\\ \partial U/\partial\theta &= 0. \qquad (49)\end{aligned}$$

Differentiating these equations with respect to $M$ and solving leads to

$$\frac{\mathrm{d}\dot{\psi}}{\mathrm{d}M} = H_{22}/\det\mathsf{H} \tag{50}$$

The matrix element $H_{22} = 2(\tilde{u}+v)a^4\dot{\psi}^4\sin^2\theta\cos^2\theta > 0$ as long as $\theta \neq 0$ and $\theta \neq \pi/2$. Therefore, the solution is stable when $\mathrm{d}\dot{\psi}/\mathrm{d}M > 0$, or $\dot{\psi}^2 > \sigma^2/3$, and unstable when $\mathrm{d}\dot{\psi}/\mathrm{d}M < 0$, or $\dot{\psi}^2 < \sigma^2/3$. An alternate route to this conclusion is to use Eq. (46) to eliminate $\theta$ from the total potential energy per length $\bar{U} = U - M\dot{\psi}$. The energy $\bar{U}$ in terms of $\dot{\psi}$ is a simple double-well potential with bias given by $m$:

$$\bar{U} = a^4\sigma^4\frac{\tilde{u}v}{\tilde{u} + v}\left[\frac{1}{4}\left(\frac{\dot{\psi}^2}{\sigma^2} - 1\right)^2 - m\frac{\dot{\psi}}{\sigma}\right]. \tag{51}$$

We now examine the behavior of the solutions. Suppose the helix is left-handed with $\kappa_2 > 0$ for $m = 0$ [$\mathrm{P}_1$ in Fig. 12(a) and (b)]. Eq. (46) has no solution for $\theta$ when $\dot{\psi}^2 < \dot{\psi}_{\mathrm{c}}^2$, where

$$\dot{\psi}_{\mathrm{c}}^2 = \pm\sigma^2 \left(1 - \frac{\tilde{u}+v}{v}\sin^2\theta_0\right) \tag{52}$$

for $\sin^2\theta_0 \lessgtr v/(\tilde{u}+v)$. When $\sin^2\theta_0 < v/(\tilde{u}+v)$, $\theta$ decreases to a minimum value of 0 as $\dot{\psi}$ decreases to $\dot{\psi}_{\mathrm{c}}$; otherwise, $\theta$ increases to a maximum value of $\pi/2$ as $\dot{\psi}$ decreases to $\dot{\psi}_{\mathrm{c}}$. If $\dot{\psi}_{\mathrm{c}}^2 > \sigma^2/3$, all these solutions are stable. This condition places a further constraint on $\theta_0$, leading to two regimes. In the regime with $0 < \sin^2\theta_0 < (2/3)v/(\tilde{u}+v)$, an applied moment $m > 0$ causes the helix to deform continuously into a *straight* twisted filament at $m = m_{\mathrm{c}}$ ($\mathrm{P}_2$ in Fig. 12); as the moment increases beyond $m_{\mathrm{c}}$, there is a discontinuous transition to a right-handed helical filament ($\mathrm{P}_3$ in Fig 12). In the regime with $(v+\tilde{u}/3)/(\tilde{u}+v) < \sin^2\theta_0 < 1$, an applied moment $m > 0$ causes the helix to deform continuously into an open coil with no twist at $m = m_{\mathrm{c}}$ ($\mathrm{Q}_2$ in Fig. 12); as the moment increases beyond $m_{\mathrm{c}}$, there is a discontinuous transition to a right-handed helical filament ($\mathrm{Q}_3$ in Fig. 12). The critical dimensionless moment is

$$m_{\mathrm{c}} = \frac{\tilde{u}+v}{v}\sin^2\theta_0\sqrt{\pm\left(1 - \frac{\tilde{u}+v}{v}\sin^2\theta_0\right)} \tag{53}$$

(again for $\sin^2\theta_0 \lessgtr v/(\tilde{u}+v)$).

If $\dot{\psi}_{\mathrm{c}}^2 < \sigma^2/3$, or equivalently, $(2/3)v/(\tilde{u}+v) < \sin^2\theta_0 < (v+\tilde{u}/3)/(\tilde{u}+v)$, then as $m$ increases, the helix becomes unstable before either the straight or coiled state is reached. Thus, there is a discontinuous transition directly from a left-handed helix to a right-handed helix at $m = m_{\mathrm{c}} = 2/(3\sqrt{3})$ (Fig 13).

The solution curves of Figs. 12 and 13 are symmetric under the combined operation $m \mapsto -m$ and $\kappa_3 \mapsto -\kappa_3$, since the nonlinear twist potential is even in $\kappa_3$ in the simple model with $\bar{v}_1 = 0$. The full model has $\bar{v}_1 \neq 0$ and therefore will not have this symmetry.

Now suppose the filament is straight when $M = 0$. In this case $\kappa_0^2 < 0$, and there is a branch of solutions corresponding to straight filaments with $\theta = 0$ and $\dot{\psi}$ given by

$$\dot{\psi}^3/\sigma^3 - (\dot{\psi}/\sigma)\cos^2\theta_0 = m\tilde{u}/(\tilde{u}+v) \tag{54}$$

The Hessian matrix for the straight solutions is diagonal, with

$$\begin{aligned} H_{11} &= va^4(3\dot{\psi}^2 - \sigma^2\cos^2\theta_0) && (55)\\ H_{22} &= a^4\dot{\psi}^2(\tilde{u}\sigma^2\sin^2\theta_0 + v\sigma^2\cos^2\theta_0 - v\dot{\psi}^2). && (56)\end{aligned}$$

Thus, the straight solutions are stable for $\dot{\psi} < \dot{\psi}_{\mathrm{h}}$, where

$$\dot{\psi}_{\mathrm{h}}^2 = \sigma^2\left(1 + \frac{\tilde{u}-v}{v}\sin^2\theta_0\right). \tag{57}$$

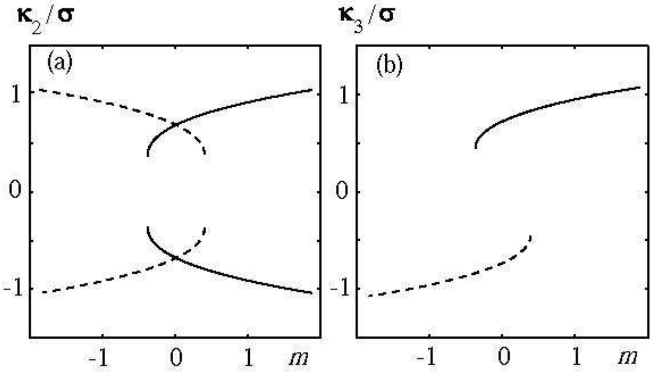

FIG. 13: (a) Signed curvature $\kappa_2$ vs. $m$ for $\tilde{u} = v$ and $\theta_0 = 43^\circ \approx 0.2389\pi$ . The dashed lines correspond to left-handed states. (b) Twist $\kappa_3$ vs. $m$ with parameters as in (a).

Equivalently, the straight states are stable for $m < m_{\mathrm{h}}$, where

$$m_{\mathrm{h}} = \frac{\tilde{u}+v}{v}\sin^2\theta_0\sqrt{1 + \frac{\tilde{u}-v}{v}\sin^2\theta_0}. \tag{58}$$

The green curves of Fig. 14 show $\kappa_2$ and $\kappa_3$ as a function of $m$.

Once $|m|$ is sufficiently large, there is also a branch of helical solutions, with $\dot{\psi}$ given by

$$\dot{\psi}^3/\sigma^3 - \cos(2\theta_0)\dot{\psi}/\sigma = m, \tag{59}$$

and $\theta$ given by

$$\sin^2\theta = \frac{v}{\tilde{u}+v} - \frac{v\cos^2\theta_0 + \tilde{u}\sin^2\theta_0}{\tilde{u}+v}\frac{\sigma^2}{\dot{\psi}^2}. \tag{60}$$

The same stability analysis described earlier, Eqs. (48–50), implies that these helical solutions are stable if and only if $\mathrm{d}\dot{\psi}/\mathrm{d}M > 0$, or $\dot{\psi}^2 > (\sigma^2/3)\cos(2\theta_0)$. Using Eq. (60) to eliminate $\theta$ from the energy leads to the potential per unit length

$$\bar{U} = a^4\sigma^4\left[\frac{1}{4}\tilde{u}\sin^4\theta_0 + \frac{1}{4}v\left(\frac{\dot{\psi}^2}{\sigma^2} - 1\right)^2 - \frac{\tilde{u}v}{\tilde{u}+v}m\frac{\dot{\psi}}{\sigma}\right]. \tag{61}$$

To determine the critical $m$ at which helical solutions are possible, note that Eq. (60) has no solution for $\theta$ when $\psi^2 < \psi_{\mathrm{h}}^2$. Therefore, the branch of helical solutions begins when $\psi = \psi_{\mathrm{h}}$ and $m = m_{\mathrm{h}}$, precisely where the straight states become unstable. The red curves of Fig. 14 show $\kappa_2$ and $\kappa_3$ for $\tilde{u} = v$ and $\theta_0 = \pi/6$. Note that since $\dot{\psi}_{\mathrm{h}}^2 > (\sigma^2/3)\cos(2\theta_0)$, the branch of helical solutions is stable.

Care must be taken in the interpretation the graphs of Fig. 14. A straight filament under external moment can destabilize via the familiar twist instability of an ordinary elastic rod [32], which is different from the polymorphic transitions studied in this article. For a rod with ends

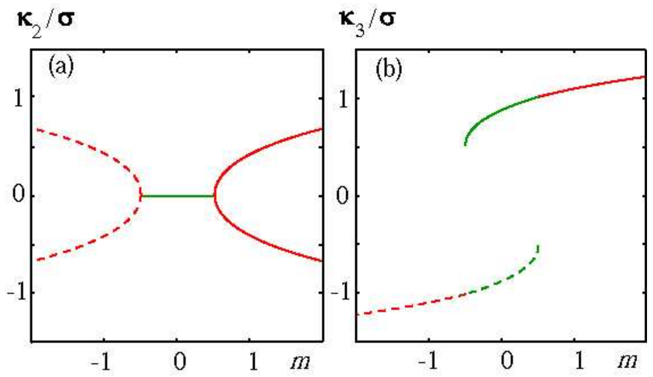

FIG. 14: (a) Signed curvature $\kappa_2$ vs. $m$ for $\tilde{u} = v$ and $\theta_0 = \pi/6$. The dashed lines correspond to left-handed states. The red curves correspond to helical solutions; the green curves correspond to straight solutions. (b) Twist $\kappa_3$ vs. $m$ with parameters as in (a).

that are not clamped, the critical moment for this instability is $M_{\text{twist}} = 2\pi A/L$, where $A$ is the bending stiffness and $L$ is the length. For our rod, $A$ is the coefficient of $\kappa_2^2$ in the energy; that is, $A = a^4\sigma^2 u \sin^2\theta_0$. Thus, we may estimate the length $L_{\text{h}}$ at which a straight rod subject the moment $m_{\text{h}}$ just sufficient to allow helical solutions will undergo the twisting instability:

$$L_{\text{h}} = 2\pi\sqrt{v/(v\Omega_{\text{p}}^2 + u\kappa_0^2)}. \tag{62}$$

Since $\kappa_0$ and $\Omega_{\text{p}}$ are of the order of microns, $L_{\text{h}}$ is about 6 microns. When $L > L_{\text{h}}$, we expect a straight flagellar filament will buckle when subject to a dimensionless moment less than $m_{\text{h}}$.

### C. Response to external force

With the simplified limit of a stiff central spring still valid, we study the response of the filament to an applied external force $F\hat{\mathbf{z}}$. As mentioned earlier, we only consider filament shapes which are either straight or helical. The line of action of the force coincides with the axis of the helix, as if there were rigid bars perpendicular to $\hat{\mathbf{z}}$ at each end of the helix (Fig. 15). Thus, the applied force also leads to an applied moment. If $\mathbf{r}(0)$ is the origin for the moment, then the applied moments at the ends of the rod are $\mathbf{r}(0) \times F\hat{\mathbf{z}} = -RF\hat{\boldsymbol{\varphi}}(0)$ at $s = 0$ and $RF\hat{\boldsymbol{\varphi}}(0)$ at $s = L$, where $\varphi$ (not to be confused with the Euler angle $\phi$) is the azimuthal coordinate and $R$ is the radius of the helix. To see that this loading condition is compatible with helical shapes, consider the equilibrium equations

$$\begin{aligned} \dot{\mathbf{M}} + \mathbf{r} \times \mathbf{F} &= \mathbf{0} & (63)\\ \dot{\mathbf{F}} &= \mathbf{0}, & (64) \end{aligned}$$

where $\mathbf{M}(s)$ is the moment due to internal stresses acting on the rod through the cross-section at $s$, and $\mathbf{F}(s)$ is the force acting on the rod through the cross-section at $s$ [32]. Since $\mathbf{F} = F\hat{\mathbf{z}}$ is constant, we can integrate the moment balance equation 63 to find $\mathbf{M} = -\mathbf{r}(s) \times \mathbf{F} + \mathbf{C}$, where $\mathbf{C}$ is an integration constant. Imposing the boundary condition $\mathbf{M}(0) = -\mathbf{r}(0) \times \mathbf{F} = RF\hat{\boldsymbol{\varphi}}(0)$ yields $\mathbf{M} = RF\hat{\boldsymbol{\varphi}}(s)$ for a helix of radius $R$. Since the moment has a constant magnitude, the constitutive relations (44) imply that helical solutions with constant curvature and torsion are possible. If the line of action of the external force passes through the end of the rod rather than the $z$ axis, then $|\mathbf{M}|$ is not uniform, and the curvature and twist are not constant.

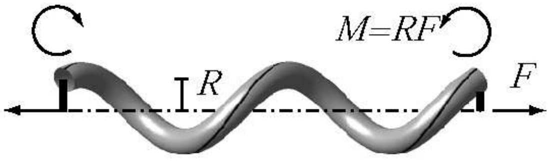

FIG. 15: The line of action of the force coincides with the axis of the helix, leading to moments applied at each end.

The principle of virtual work for our loading condition is

$$\begin{aligned} \delta E \;&-\; \mathbf{F} \cdot [\delta\mathbf{r}(L) - \delta\mathbf{r}(0)] \\ &-\; [\mathbf{M}(L) \cdot \delta\boldsymbol{\Upsilon}(L) - \mathbf{M}(0) \cdot \delta\boldsymbol{\Upsilon}(0)] = 0, \end{aligned} \tag{65}$$

where $\mathbf{M}(s) = RF\hat{\boldsymbol{\varphi}}(s)$ and $\delta\Upsilon_\mu = \epsilon_{\mu\nu\lambda}\delta\hat{\mathbf{e}}_\nu \cdot \hat{\mathbf{e}}_\lambda$ as defined before. To express Eq. (65) in terms of the variables $\psi$, $\theta$, and $\phi$, first use $\hat{\mathbf{z}} \cdot [\mathbf{r}(s) - \mathbf{r}(0)] = \int_0^L \hat{\mathbf{e}}_3 \cdot \hat{\mathbf{z}} \mathrm{d}s$ to write

$$-\mathbf{F} \cdot [\delta\mathbf{r}(L) - \delta\mathbf{r}(0)] = F\int_0^L \sin\theta\delta\theta \mathrm{d}s. \tag{66}$$

Then use the relation $\hat{\boldsymbol{\varphi}} = -\cos\theta\hat{\mathbf{e}}_2 + \sin\theta\hat{\mathbf{e}}_3$ and Eqs. (29) and (30) to write $\mathbf{M} \cdot \delta\boldsymbol{\Upsilon}$ in terms of $\psi$, $\theta$, and $\phi$. Just as in the case of an applied external moment, the Euler-Lagrange equations eventually imply $\dot{\phi} = 0$, and we take $\phi = \pi/2$. Thus,

$$[\mathbf{M}(L) \cdot \delta\boldsymbol{\Upsilon}(L) - \mathbf{M}(0) \cdot \delta\boldsymbol{\Upsilon}(0)] = \left[F\frac{\sin^2\theta}{\dot{\psi}}\right]_0^L. \tag{67}$$

Carrying out steps analogous to those that led to Eqs. (32–38) and specializing to the case of a helix leads to

$$\begin{aligned} \dot{\psi}^2\left(\dot{\psi}^2\sin^2\theta - \kappa_0^2\right) &= -\frac{F}{\tilde{u}a^4}\cos\theta & (68)\\ \dot{\psi}^2\cos\theta\left(\dot{\psi}^2\cos^2\theta - \Omega_{\text{p}}^2\right) &= \frac{F}{va^4}\sin^2\theta. & (69) \end{aligned}$$

Note that these equations also follow directly from the constitutive relations of Eq. (44), $M_1 = 0$, $M_2 = -RF\cos\theta$, and $M_3 = RF\sin\theta$.

We were unable to find an analytic solution to Eqs. (68) and (69). Instead, we used a numerical continuation method to generate the solutions $\dot{\psi}$ and $\theta$ as a function

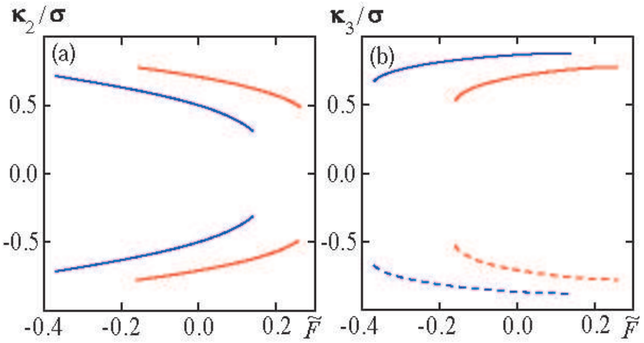

FIG. 16: (a) Signed curvature $\kappa_2$ vs. $\tilde{F}$ for $\tilde{u} = v$, and $\theta_0 = \pi/6$ (blue curves) and $\theta_0 = \pi/4$ (red curves). The dashed lines correspond to left-handed states. (b) Twist $\kappa_3$ vs. $\tilde{F}$ with parameters as in (a).

of $F$ [37]. The advantage of the continuation method is that it can negotiate turning points such as those in the graph of $\kappa_3$ vs. $\bar{v}_1$ in Fig. 8. The results of our numerical calculation are shown in Fig. 16, where we have introduced the dimensionless force $\tilde{F} = F/(\tilde{u}a^4\sigma^4)$. Figure 16 shows that uniform helical solutions only exist in a finite range of $\tilde{F}$. To see that Eqs. (68) and (69) do not have solutions for large $F$, consider their asymptotic form at large $F$:

$$\dot{\psi}^4 \sim -\frac{F}{\tilde{u}a^4}\cos\theta \tag{70}$$

$$\dot{\psi}^4\cos\theta \sim \frac{F}{va^4}\sin^2\theta. \tag{71}$$

The ratio of these two equations simplifies to $\tan^2\theta \sim -v/\tilde{u}$, which is impossible since $\tilde{u} > 0$ and $v > 0$. We speculate that the filament takes a non-uniform shape with varying curvature and twist for values of $\tilde{F}$ outside the allowed range of Fig. 16. Note that for a given force $\tilde{F}$ and a given signed curvature $\kappa_2$, there are both left-handed and right-handed filaments of same magnitude of twist owing to symmetry of the energy function in the simplified version of the model; therefore the solid and dashed lines overlap in Fig. 16(a).

We do not discuss the case of an otherwise *straight* filament subject to external force, since in this case we found no examples of transitions from straight to helical states.

## V. FULL MODEL

In this section, we consider the full model, which accounts for the inextensibility of the filament and the lateral bonds between protofilaments. We follow the same analysis used for the simple model. The twist-stretch coupling arising from lateral bonds, Eq. (8), makes the phase diagram for ground states in the full model qualitatively different from the phase diagram for ground states in the simple model (Fig. 2 of [14]). However, the response of the filament to external moment and external force in the full model is very similar to the response in the simple model.

### A. Ground states

The full model includes all the terms of the energy (16), which we write as $E = \int V\mathrm{d}s$, where $V = U_0 + U_\mathrm{s} + U_\mathrm{t} + U_5 + U_\mathrm{c}$ and we note again that to a good approximation, $\mathrm{d}S \approx \mathrm{d}s$. As in the analysis of the simple model, the cooperative term is minimized when $\kappa_1 = 0$. Assuming helical or straight states and minimizing $V$ over $\epsilon$, $\kappa_2$, and $\kappa_3$, we find

$$\frac{\epsilon^3}{\epsilon_\mathrm{p}^3} + \frac{c_1\epsilon}{\epsilon_\mathrm{p}} - c_2 - \frac{\bar{k}_5\gamma\kappa_3}{\Omega_\mathrm{p}} + \frac{3\gamma^2\epsilon\kappa_2^2}{2\epsilon_\mathrm{p}\Omega_\mathrm{p}^2} = 0 \tag{72}$$

$$\frac{3\epsilon^2\kappa_2}{2\epsilon_\mathrm{p}^2\Omega_\mathrm{p}} - \frac{\kappa_2}{2\Omega_\mathrm{p}} + \frac{3\gamma^2\kappa_2^3}{8\Omega_\mathrm{p}^3} = 0 \tag{73}$$

$$\frac{v}{11u}\gamma^3\left(\frac{\kappa_3^3}{\Omega_\mathrm{p}^3} - \frac{\kappa_3}{\Omega_\mathrm{p}} - \bar{v}_1\right) - \frac{\bar{k}_5\epsilon}{\epsilon_\mathrm{p}} = 0, \tag{74}$$

where $c_1 = 2\bar{k}_\mathrm{s} - 1$, $\bar{k}_\mathrm{s} = k_\mathrm{s}/(22u\epsilon_\mathrm{p}^2)$, $c_2 = 2\bar{k}_\mathrm{s}\epsilon_0/\epsilon_\mathrm{p} + \bar{u}_1$, $\bar{u}_1 = u_1/(u\epsilon_\mathrm{p})$, $\bar{k}_5 = k_5/(11u\epsilon_\mathrm{p}^2)$, and $\gamma = a\Omega_\mathrm{p}/\epsilon_\mathrm{p}$. In this section, we choose representative values $\gamma = 1.8$, $\tilde{u} = v$, $\bar{k}_5 = 1$ and $\bar{u}_1 = -0.5$ to illustrate the predictions of our model. When $k_5 \neq 0$, there will be no discontinuous transitions between helices of opposite handedness if $\bar{k}_\mathrm{s}$ is too small; hence, we choose the relatively large value $\bar{k}_\mathrm{s} = 8$. The two parameters $\bar{v}_1$ and $c_2$ are the molecular switches of the full model, just as $\bar{v}_1$ and $\epsilon_0/\epsilon_\mathrm{p}$ are the switches of the simple model: positive $\bar{v}_1$ favors right-handed twist, and positive $c_2$ favors longer protofilaments. Equation (73) shows that there are straight solutions with $\kappa_2 = 0$ and curved solutions with $\kappa_2 \neq 0$, just as in the simple model. Evaluation of the Hessian using the independent variables $\epsilon$, $\kappa_3$, and $\kappa_2$ for the straight states shows that they are unstable for $\epsilon^2 < \epsilon_\mathrm{p}^2/3$. Solving Eqs. (72) and (74) for $\bar{v}_1$ and $c_2$ when $\kappa_2 = 0$ and $\epsilon = \pm\epsilon_\mathrm{p}/\sqrt{3}$ yields the boundaries between the straight and the curved states shown in the phase diagram of Fig. 17. The phase diagram also shows the regions of metastability (the purple, blue, yellow, and brown regions), where there is more than one equilibrium solution to Eqs. (72–74). We found the boundaries of these regions by brute force; we systematically varied $\bar{v}_1$ and $c_2$, solving the equilibrium equations for each pair of values and noting when the number of solutions changed. The twist-stretch coupling $k_5$ tilts the total region of metastability, whereas in the simple model the region of metastability is vertical, $\bar{v}_1^2 < 4/27$ (see Fig 2 of [14]). The phase diagram also has a dotted line showing where the two possible solutions of left-handed and right-handed filaments have equal energy.

The full model yields many possibilities for transitions, including discontinuous transitions between straight

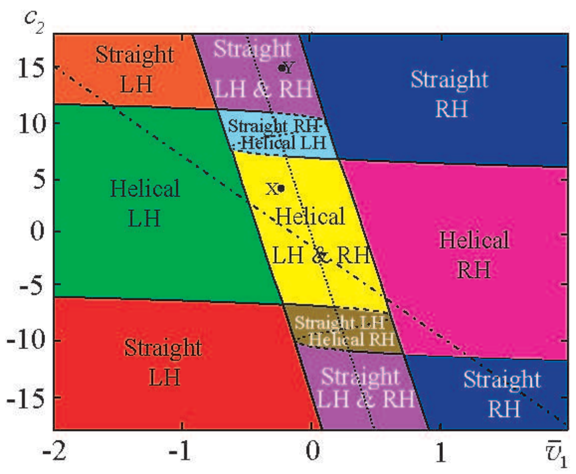

FIG. 17: Phase diagram for $\gamma = 1.8$, $\tilde{u} = v$, $\bar{k}_s = 8$, $\bar{k}_5 = 1$ and $\bar{u}_1 = -0.5$; $\bar{v}_1$ and $c_2$ are dimensionless. The inclined dotted line defines the boundary where the energy of the left-handed state equals the energy of the right-handed state. The diagonal dash-dot line traces out the values of $\bar{v}_1$ and $c_2$ used to calculate the curvature vs. twist plot of Fig. 18. The points X and Y in the metastable regions represent the corresponding parameters used for evaluating the response of a helical and straight filament to external loading respectively.

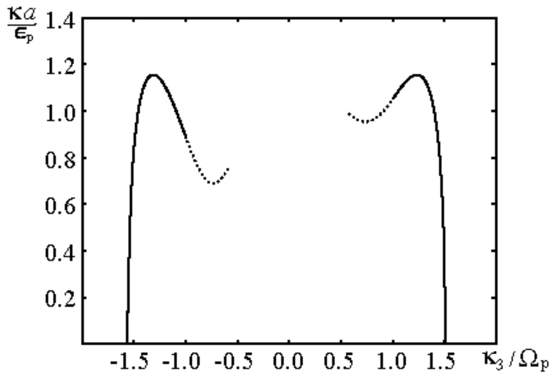

FIG. 18: Curvature vs. twist, in dimensionless units, for $\gamma = 1.8$, $\tilde{u}/v = 1$, $\bar{k}_s = 8$, $\bar{k}_5 = 1$ and $\bar{u}_1 = -0.5$. The parameters $\bar{v}_1$ and $c_2$ vary along the dash-dot line of Fig. 17. The dotted lines corresponds to metastable states for which the lower energy states are of opposite handedness.

states of opposite handedness, discontinuous transitions between helical states of opposite handedness, and continuous transitions between straight states and helical states of the same handedness. These transitions are present in the simple model. The full model also predicts discontinuous transitions from a straight state to a helical state of opposite handedness, which do not occur in the simple model.

As mentioned above, changes in solvent condition change the values of the material parameters. To illustrate this effect, in Fig. 18 we plot $\kappa$ vs. $\kappa_3$ for values of $(\bar{v}_1, c_2)$ along the dashed line of Fig. 17. There is a simultaneous jump in curvature and twist of the filament. Note that $\kappa$ rises so steeply with twist that $\kappa$ may appear to be undergoing an abrupt jump with small changes in parameters. We also point out that the value of $\gamma$ determines the maximum pitch angle that can be attained by the helical filament. Changing the value of $\gamma = a\Omega_p/\epsilon_p$ amounts to changing the relative positions of the minima in the nonlinear potentials (2) and (7). If $\gamma$ is small, there is a wider range of possible pitch angles. We chose $\gamma = 1.8$ for Figs. 17 and 18, which gives a maximum pitch angle of about 35°. Higher pitch angle polymorphs such as curly I and curly II require lower values of $\gamma$.

### B. Response to moment and force

We now consider the response of a filament to external moment and force in the full model. Since the filament is extensible, there is an additional contribution to the expression (66) for the work done by an external force:

$$\mathbf{F}\cdot[\delta\mathbf{r}(L) - \delta\mathbf{r}(0)] = -F\int_0^L (\sin\theta\delta\theta - \cos\theta\delta\epsilon)\,\mathrm{d}s, \quad (75)$$

where we have used the approximation $\mathrm{d}S \approx \mathrm{d}s$. In addition to the Euler-Lagrange equations derived for external moment in the simple model, Eqs. (32–38), suitably modified to include both an external moment and force, there is a new equation corresponding to the stretch degree of freedom $\epsilon$,

$$\frac{\partial V}{\partial \epsilon} - \frac{\mathrm{d}}{\mathrm{d}s}\frac{\partial V}{\partial \dot{\epsilon}} - F\cos\theta = 0, \quad (76)$$

as well as natural boundary conditions

$$\left[\frac{\partial V}{\partial \dot{\epsilon}}\right]_{s=0} = \left[\frac{\partial V}{\partial \dot{\epsilon}}\right]_{s=L} = 0. \quad (77)$$

The argument leading to $\dot{\phi} = 0$ in the simple model applies here as well, leading to

$$\begin{aligned}
\frac{\epsilon^3}{\epsilon_p^3} + c_1\frac{\epsilon}{\epsilon_p} - c_2 - \frac{\bar{k}_5\gamma\dot{\psi}\cos\theta}{\Omega_p} + g_1 &= \bar{F}\epsilon_p\cos\theta \quad (78)\\
\frac{\dot{\psi}\sin\theta}{\Omega_p}\left(\frac{\bar{k}_5\gamma\epsilon}{\epsilon_p} - g_2 + g_3\cos\theta\right) &= -\bar{F}\sin\theta \quad (79)\\
g_2\cos\theta - \frac{\bar{k}_5\gamma\epsilon}{\epsilon_p}\cos\theta + g_3\sin^2\theta &= \bar{M} \quad (80)
\end{aligned}$$

where $\bar{F} = F/(11u\epsilon_p^4)$, $\bar{M} = M\Omega_p/(11u\epsilon_p^4)$, and

$$\begin{aligned}
g_1 &= (3\gamma^2\epsilon\dot{\psi}^2\sin^2\theta)/(2\epsilon_p\Omega_p^2) \quad (81)\\
g_2 &= \frac{v\gamma^4}{11u}\left[\frac{\dot{\psi}\cos\theta}{\Omega_p}\left(\frac{\dot{\psi}^2\cos^2\theta}{\Omega_p^2} - 1\right) - \bar{v}_1\right] \quad (82)\\
g_3 &= \frac{\gamma^2\dot{\psi}}{8\Omega_p}\left(-4 + \frac{12\epsilon^2}{\epsilon_p^2} + \frac{3\gamma^2\dot{\psi}^2\sin^2\theta}{\Omega_p^2}\right). \quad (83)
\end{aligned}$$

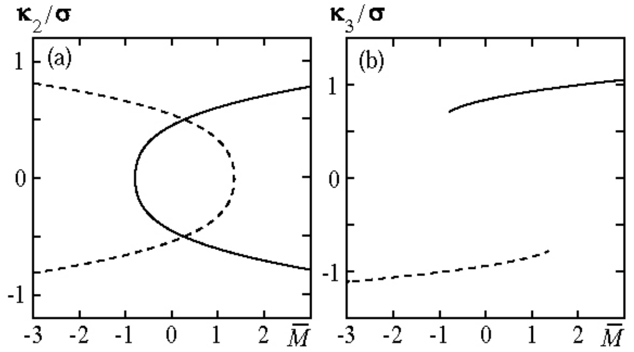

FIG. 19: (a) Signed curvature $\kappa_2$ vs. $\bar{M}$ for $\tilde{u} = v$, $\bar{k}_s = 8$, $\bar{k}_5 = 1$, $c_2 = 4$, $\bar{v}_1 = -0.25$, and $\bar{u}_1 = -0.5$. The dashed lines correspond to left-handed states. (b) Twist $\kappa_3$ vs. $\bar{M}$ with parameters as in (a).

We use the numerical continuation method to solve these equations for the cases of applied moment with $\bar{F} = 0$, and applied force with $\bar{M} = 0$. We use the values of $\bar{v}_1$ and $c_2$ corresponding to the point X in Fig. 17, and the same parameter values for $\gamma$, $\tilde{u}$, $v$, $\bar{k}_s$, $k_5$, and $\bar{u}_1$ used in section IV. The point X corresponds to a stable left-handed normal helix, and a metastable right-handed helix; we study the response of the left-handed helix. Figure 19 shows that the left-handed helical filament changes its shape smoothly with increasing moment, going through helical metastable states until is straightens out, and then abruptly changes to a right-handed filament. Note the qualitative similarity with the predictions of the simple model, Fig. 12. An important difference is that the asymmetry of the potential in the full model favors one handedness over the other; for example, at $M = 0$, the right-handed solution of the full model has higher energy than the left-handed solution.

The response to moment of a filament which is straight when $M = 0$ is shown in Fig. 20. The parameters $\bar{v}_1$ and $c_2$ are chosen to correspond to the point Y in Fig. 17, which represents a stable right-handed straight filament. At these parameter values there is also a metastable left-handed straight filament. As the moment increases from zero, the twist increases until eventually the straight filament destabilizes at a critical torque, and there is a continuous transition to a right-handed helix. When the moment decreases from zero, the straight filament untwists and and a left-handed helix forms at a critical torque. Due to the asymmetry of the potential for these parameter values, the interval of moments for which left-handed straight filaments exist is a subset of the interval of moments for which right-handed straight filaments exist. Nevertheless, Fig. 20 is qualitatively similar to Fig. 14.

Finally, Fig. 21 shows the response of the left-handed filament at X to an applied force, showing the same qualitative features we found in the simple model, Fig. 16.

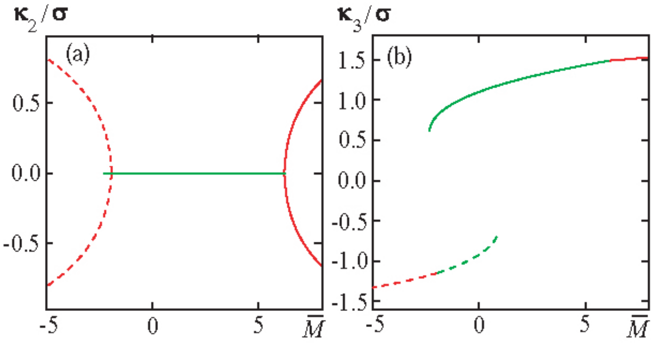

FIG. 20: (a) Signed curvature $\kappa_2$ vs. $\bar{M}$ for $\tilde{u} = v$, $\bar{k}_s = 8$, $\bar{k}_5 = 1$, $c_2 = 15$, $\bar{v}_1 = -0.25$, and $\bar{u}_1 = -0.5$. The red and green curves indicate the helical and straight filaments, respectively. The dashed lines correspond to left-handed states. (b) Twist $\kappa_3$ vs. $\bar{M}$ with parameters as in (a).

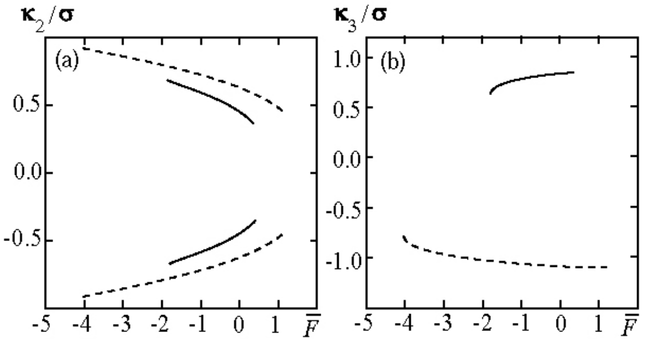

FIG. 21: (a) Signed curvature $\kappa_2$ vs. $\bar{F}$ for $\tilde{u} = v$, $\bar{k}_s = 8$, $\bar{k}_5 = 1$, $c_2 = 15$, $\bar{v}_1 = -0.25$, and $\bar{u}_1 = -0.5$. The dashed lines correspond to left-handed states. (b) Twist $\kappa_3$ vs. $\bar{F}$ with parameters as in (a).

## VI. DISCUSSION AND CONCLUSION

We have introduced a new coarse-grained model for polymorphic transitions in bacterial flagella. The key elements of the model are a double-well potential for protofilament stretch, a double-well potential for twist arising from lateral interactions between neighboring protofilaments, elastic mismatch between the protofilaments and the inner core, and cooperative interactions between subunits on the same protofilament. Motivated by the chiral structure of flagellar filaments, we have also included a potential energy for twist-stretch coupling in the full version of our model. This potential energy is in marked contrast with the tight coupling between filament twist and protofilament stretch assumed in [26] and [29], which leads to a discrete set of possible values for the curvature and twist of a filament in the absence of loading. Our softer coupling in the full model ($k_5 \neq 0$) and complete decoupling ($k_5 = 0$) in the simple model lead to a continuous variation of curvature and twist as a function of the material parameters, with discontinuous transitions only at special critical values. Our prediction calls for new single-molecule experiments in which the shape of a *single* filament is observed as solvent conditions are carefully varied.

The main result of our work is the calculation of the response of a polymorphic filament to moments and forces applied at the ends. In the simplified version of our theory, the assumption of a stiff central core leads to semi-analytic formulas for the shape as a function of moment. These formulas allowed us to reveal a host of possible distinct scenarios, such as the moment-driven continuous unwinding of a helical filament to a straight shape, followed by an abrupt transition to a helix of opposite handedness as the moment increases (Fig. 12, blue curves). Another important generic prediction of our model is that the curvature and the twist both jump at the same critical value of moment. Although our model makes clear predictions for the qualitative behavior of filaments, a critical requirement for testing the quantitative validity of our theory is the determination of the values of the material parameters such as $u$, $v$, $\bar{v}_1$, and $\epsilon_0$. These may be measured by bending and twisting straight filaments, or perhaps may be computing using the techniques developed in [38]. We can make a rough order-of-magnitude estimate of the moment required to cause a polymorphic transformation by observing that the critical moment in the simple model is approximately $M \approx u a^4 \kappa_0^2$, where we have assumed for simplicity that $u \approx v$, $\kappa_0 \approx \Omega_{\rm p}$, $\sigma \approx \kappa_0^2$, and we have also dropped overall numerical factors (such as the distinction between $u$ and $\tilde{u}$). Since the bending stiffness $A \approx u a^4 \kappa_0^2$, we may write $M \approx A\kappa_0$ for the characteristic moment. Using $\kappa_0 \approx 1\,\mu\mathrm{m}$, $A \approx 10^{-24}\,\mathrm{Nm}^2$ (see [39] and references therein) yields a characteristic torque for polymorphic transition of $10^{-18}\,\mathrm{Nm}$. This torque is comparable to the hydrodynamic torque experienced by a rotating flagellum, which we can estimate by computing the the torque on the cell body. Assuming the cell body rotates at $\omega = 10\,\mathrm{Hz}$ [40] and is a sphere of radius $R = 1\,\mu\mathrm{m}$ leads to a hydrodynamic torque of the order of $M = 8\pi\eta R^3\omega \approx 10^{-18}\,\mathrm{Nm}$ [41]. These values match well with those of Hotani, who estimated the orders of magnitude for the transformation of a normal to semi-coiled filament to be $10^{-18}\,\mathrm{Nm}$, and $10^{-19}\,\mathrm{Nm}$ for the reverse transformation [9].

The shape-moment curves predicted by our theory may be readily tested by new micromanipulation experiments in which a filament is subject to prescribed moments or forces. It would also be interesting to vary the solvent conditions while doing these measurements. Also, since our theory makes predictions about the sign of $\kappa_2$, it would be useful to experimentally track the sign of $\kappa_2$ during a transition. For example, for a transition such as is depicted in Fig. 13(a), a bead which is stuck to a protofilament which is on the inside of the helix before the transition would end up on the outside afterwards.

Our theory also suggests new directions for theoretical work. In this article we have considered boundary conditions of fixed moment or force. If instead we fixed the positions and orientations of the ends of the filament ("hard boundary conditions"), then the filament could take on a shape in which two different polymorphic states coexist (see Fig. 1(a) of [30] for a similar experimental example with *free* filaments with subunits of mixed type). We could use our theory to analyze these states, generalizing the calculations for planar beams with a bistable potential for curvature carried out in [42]. Another important generalization of our theory would be to study the dynamics of polymorphic transitions, which has been studied in the context of a different continuum model in [30] and [31]. Finally, it is natural to attempt to go beyond our protofilament-based picture and treat every subunit on equal footing, and try to adapt ideas developed for understanding martensitic transformations to polymorphic flagella [43].

## Acknowledgments

We thank H. Berg, C. Calladine, D. DeRosier, A. Goriely, K. Namba, A. Needleman, L. Turner, and C. Wolgemuth for helpful conversations. We are especially grateful to Greg Huber for many important early discussions. We thank C. Wolgemuth for providing the code used to generate Fig. 5 and other figures. This work is supported in part by National Science Foundation grants CMS-0093658 and NIRT-0404031, and the Brown University MRSEC. TRP thanks the Aspen Center for Physics for hospitality while some of this work was completed.

## APPENDIX A: EULER ANGLES

The sequence of rotations defining the Euler angles is described in section IV B. Carrying out these rotations on the initial frame $\{\hat{\mathbf{x}}, \hat{\mathbf{y}}, \hat{\mathbf{z}}\}$ leads to

$$\hat{\mathbf{e}}_1' = \cos\psi\hat{\mathbf{x}} + \sin\psi\hat{\mathbf{y}} \tag{A1}$$

$$\hat{\mathbf{e}}_2' = -\sin\psi\hat{\mathbf{x}} + \cos\psi\hat{\mathbf{y}} \tag{A2}$$

$$\hat{\mathbf{e}}_3' = \hat{\mathbf{z}}, \tag{A3}$$

then

$$\hat{\mathbf{e}}_1'' = \cos\psi\cos\theta\hat{\mathbf{x}} + \sin\psi\cos\theta\hat{\mathbf{y}} - \sin\theta\hat{\mathbf{z}} \tag{A4}$$

$$\hat{\mathbf{e}}_2'' = -\sin\psi\hat{\mathbf{x}} + \cos\psi\hat{\mathbf{y}} \tag{A5}$$

$$\hat{\mathbf{e}}_3'' = \cos\psi\sin\theta\hat{\mathbf{x}} + \sin\psi\sin\theta\hat{\mathbf{y}} + \cos\theta\hat{\mathbf{z}}, \tag{A6}$$

and finally

$$\begin{aligned} \hat{\mathbf{e}}_1 &= (-\sin\psi\sin\phi + \cos\psi\cos\phi\cos\theta)\hat{\mathbf{x}} \\ &+ (\cos\psi\sin\phi + \sin\psi\cos\phi\cos\theta)\hat{\mathbf{y}} \\ &- \cos\phi\sin\theta\hat{\mathbf{z}} \end{aligned} \tag{A7}$$

$$\begin{aligned} \hat{\mathbf{e}}_2 &= -(\sin\psi\cos\phi + \cos\psi\sin\phi\cos\theta)\hat{\mathbf{x}} \\ &+ (\cos\psi\cos\phi - \sin\psi\sin\phi\cos\theta)\hat{\mathbf{y}} \\ &+ \sin\phi\sin\theta\hat{\mathbf{z}} \end{aligned} \tag{A8}$$

$$\hat{\mathbf{e}}_3 = \cos\psi\sin\theta\hat{\mathbf{x}} + \sin\psi\sin\theta\hat{\mathbf{y}} + \cos\theta\hat{\mathbf{z}}. \tag{A9}$$

Plugging Eqs. (A7–A9) into Eq. (4), $\mathrm{d}\hat{\mathbf{e}}_\mu/\mathrm{d}s = \boldsymbol{\kappa} \times \hat{\mathbf{e}}_\mu$, yields Eqs. (24–26), which show that the $\kappa_\mu$ depend on $\theta$, $\phi$, $\dot{\psi}$, and $\dot{\phi}$. Furthermore,

$$\kappa^2 = \dot{\theta}^2 + \sin^2\theta\dot{\psi}^2 \qquad \text{(A10)}$$

and

$$\begin{aligned}\dot{\kappa}_1^2 + \dot{\kappa}_2^2 \ &= \ \sin^2\theta\dot{\phi}^2\dot{\psi}^2 + \dot{\theta}^2\left(\dot{\phi} - \cos\theta\dot{\psi}\right)^2 \\ &+ \ 2\sin\theta\dot{\phi}\dot{\psi}\ddot{\theta} + \ddot{\theta}^2 \\ &- \ 2\sin\theta\dot{\theta}\left(\dot{\phi} - \cos\theta\dot{\psi}\right)\ddot{\psi} + \sin^2\theta\ddot{\psi}^2 \text{(A11)}\end{aligned}$$

Therefore, $\kappa^2$ and $\dot{\kappa}_1^2 + \dot{\kappa}_2^2$ are both independent of $\psi$, $\phi$, and $\ddot{\phi}$. Since $\kappa_3$ is also independent of these variables [see Eq. (26)], the energy density $U$ is also.

[1] W.A. Eaton, E.R. Henry, J. Hofrichter, and A. Mozzarelli, Nature Struct. Biol. **6**, 351 (1999).

[2] C.L. Lawson and P.B. Sigler, Nature **333**, 869 1988.

[3] K.L. Krause, K.W. Volz, and W.N. Lipscomb, Proc. Natl. Acad. Sci. USA **82**, 1643 (1985).

[4] D. Bray and T. Duke, Annu. Rev. Biophys. Biomol. Struct. **33**, 53 (2004).

[5] R.M. Macnab, In *Eschericia coli and Salmonella*, edited by F.C. Neidhardt *et al.*, (American Society for Microbiology, Washington, D.C., 1996), pp. 123.

[6] S. Asakura, Advan. in Biophys. **1**, 99 (1970).

[7] L. Turner, W.S. Ryu, and H.C. Berg, J. Bacteriol. **182**, 2793 (2000).

[8] R.M. Macnab and M.K. Ornston, J. Mol. Biol. **112**, 1 (1977).

[9] H. Hotani, J. Mol. Biol. **156**, 791 (1982).

[10] H.C. Berg, *E. coli in Motion* (Springer-Verlag, New York, 2004).

[11] M.J. Kim, J.C. Bird, A.J. Van Parys, K.S. Breuer, and T.R. Powers, Proc. Natl. Acad. Sci. USA **100**, 15481 (2003).

[12] R. Kamiya and S. Asakura, J. Mol. Biol. **106**, 167 (1976).

[13] K. Hasegawa, R. Kamiya, and S. Asakura, J. Mol. Biol. **160**, 609 (1982).

[14] S.V. Srigiriraju and T.R. Powers, Phys. Rev. Lett. **94**, 248101 (2005).

[15] I. Yamashita, K. Hasegawa, H. Suzuki, F. Vonderviszt, Y. Mimori-Kiyosue, and K. Namba, Nature Struct. Biol. **5**, 125 (1998).

[16] F.H.C. Crick and J.D. Watson, Nature **177**, 473 (1956).

[17] H. Fraenkel-Conrat and R.C. Williams, Proc. Natl. Acad. Sci. USA **41**, 690 (1955).

[18] H.C. Hyman and S. Trachtenberg, J. Mol. Biol. **220**, 79 (1991).

[19] Y. Mimori, I. Yamashita, K. Murata, Y. Fujiyoshi, K. Yonekura, C. Toyoshima, and K. Namba, J. Mol. Biol. **249**, 69 (1995).

[20] K. Yoshioka, S. Aizawa, and S. Yamaguchi, J. Bacteriol. **177**, 1090 (1995).

[21] S. Kanto, H. Okino, S.I. Aizawa, and S. Yamaguchi, J. Mol. Biol. **219**, 471 (1991).

[22] Y. Mimori-Kiyosue, F. Vonderviszt, I. Yamashita, Y. Fujiyoshi, and K. Namba, Proc. Natl. Acad. Sci. USA **93**, 15108 (1996).

[23] F. Vonderviszt, S.I. Aizawa, and K. Namba, J. Mol. Biol. **221**, 1461 (1991).

[24] F.A. Samatey, K. Imada, S. Nagashima, F. Vonderviszt, T. Kumasaka, M. Yamamoto, and K. Namba, Nature **410**, 331 (2001).

[25] K. Yonekura, S. Maki-Yonekura, and K. Namba, Nature **424**, 643 (2003).

[26] C.R. Calladine, Nature **255**, 121 (1975).

[27] C.R. Calladine, J. Theoret. Biol. **57**, 469 (1976).

[28] C.R. Calladine, J. Mol. Biol. **118**, 457 (1978).

[29] K. Hasegawa, I. Yamashita, and K. Namba, Biophys. J. **74**, 569 (1998).

[30] R.E. Goldstein, A. Goriely, G. Huber, and C. W. Wolgemuth, Phys. Rev. Lett. **84**, 1631 (2000).

[31] D. Coombs, G. Huber, J.O. Kessler, and R.E. Goldstein, Phys. Rev. Lett. **89**, 118102 (2002).

[32] L.D. Landau and E.M. Lifshitz, *Theory of Elasticity* (Pergamon Press, Oxford, 1986).

[33] J.F. Marko and E.D. Siggia, Macromolecules **27**, 981 (1994).

[34] K. Namba and F. Vonderviszt, Q. Rev. Biophys. **30**, 1 (1997).

[35] R.D. Kamien, Rev. Mod. Phys. **74**, 953 (2002).

[36] A.E.H. Love, *A treatise on the mathematical theory of elasticity* (Dover Publications, New York, 4th edition, 1944).

[37] H. B. Keller, *Numerical solution of bifurcation and nonlinear eigenvalue problems, in Applications of bifurcation theory*, edited by P. H. Rabinowitz, (Academic Press, New York, 1977).

[38] T.C. Flynn and J.P. Ma, Biophys. J. **86**, 3204 (2004).

[39] M.J. Kim and T.R. Powers, Phys. Rev. E **71**, 021914 (2005).

[40] R.M. Macnab, Proc. Natl. Acad. Sci. USA **74**, 221 (1977).

[41] L.D. Landau and E.M. Lifshitz, *Fluid Mechanics* (Butterworth-Heinemann Ltd., Oxford, 2nd edition, 1987).

[42] R.D. James, J. Elasticity **11**, 239 (1981).

[43] K. Bhattacharya, *Microstructure of Martensite* (Oxford University Press, Oxford, 2004).